Received: 25 April 2025 | Revised: 11 June 2025 | Accepted: 29 June 2025

DOI: 10.1002/pro.70228

REVIEW ARTICLE

THE PROTEIN SOCIETY WILEY

Exploring binding and allosteric energy landscapes for the KRAS interactions with effector proteins using Markov state modeling of conformational ensembles and allosteric network modeling

Sian Xiao[1] | **Mohammed Alshahrani**[2] | **Guang Hu**[3,4] | **Peng Tao**[1] | **Gennady Verkhivker**[2,5]

[1]Department of Chemistry, Center for Research Computing, Center for Drug Discovery, Design, and Delivery (CD4), Southern Methodist University, Dallas, Texas, USA

[2]Keck Center for Science and Engineering, Schmid College of Science and Technology, Chapman University, Orange, California, USA

[3]Department of Bioinformatics and Computational Biology, School of Life Sciences, Suzhou Medical College of Soochow University, Suzhou, China

[4]Jiangsu Province Engineering Research Center of Precision Diagnostics and Therapeutics Development, Soochow University, Suzhou, China

[5]Department of Biomedical and Pharmaceutical Sciences, Chapman University School of Pharmacy, Irvine, California, USA

Correspondence
Gennady Verkhivker, Keck Center for Science and Engineering, Schmid College of Science and Technology, Chapman University, Orange, CA 92866, USA.
Email: verkhivk@chapman.edu

Funding information
National Institutes of Health, Grant/Award Numbers: 1R01AI181600-01, 6069-SC24-11, R15GM122013; Kay Family Foundation, Grant/Award Number: A20-0032

Review Editor: Lynn Kamerlin

Abstract

Kirsten rat sarcoma viral oncogene homolog (KRAS) is a pivotal oncoprotein that regulates cell proliferation and survival through interactions with downstream effectors such as RAF1. Despite significant advances, the dynamic and energetic mechanisms of KRAS allostery by which oncogenic mutations can modulate KRAS-RAF1 signaling remain poorly understood. In this study, we employ microsecond molecular dynamics simulations, mutational scanning, and binding free energy calculations together with dynamic network modeling to elucidate the effect of KRAS G12V, G13D, and Q61R mutations and characterize the thermodynamic drivers and hotspots of KRAS binding and allostery. We found that these mutations stabilize the active state and enhance RAF1 binding by differentially modulating the flexibility of switch regions. The G12V mutation rigidifies both switch I and switch II, locking KRAS in a stable active state. In contrast, the G13D mutation moderately reduces switch I flexibility, while the Q61R mutation induces a more dynamic conformational landscape. Mutational scanning and binding free energy analysis of KRAS-RAF1 complexes identified key binding affinity hotspots that leverage synergistic electrostatic and hydrophobic binding interactions in stabilizing the KRAS-RAF1 interfaces. Dynamic network analysis identifies critical allosteric centers and a conserved allosteric architecture that mediate long-range interactions in the KRAS-RAF1 complexes and enable precision modulation of KRAS dynamics in oncogenic contexts. The predictions accurately reproduced the experimental data on KRAS allostery and provided a detailed map of allosteric communications mediated by the central β-sheet region of KRAS that connects the binding interface hotspots with allosteric hubs transmitting functional conformational changes. Together, these findings advance our understanding of mechanisms underlying allosteric regulation of KRAS binding and underscore the importance of targeting mutant-specific conformations for therapeutic interventions.

KEYWORDS
allosteric mechanism, binding energetics, computer simulations, effector proteins, integrative protein modeling, KRAS protein, markov state models, molecular dynamics, mutational scanning, protein network analysis

1 | INTRODUCTION

The GTPase Kirsten rat sarcoma viral oncogene homolog (KRAS) is a critical oncogene that is mutated in many human cancers (Alawieh et al., 2024; Lee et al., 2022; Prior et al., 2020; Timar & Kashofer, 2020; Yang et al., 2023). KRAS alternates between two conformational states: an inactive guanosine diphosphate (GDP)-bound state and an active guanosine triphosphate (GTP)-bound state. This transition is tightly regulated by guanine nucleotide exchange factors (GEFs), which promote the exchange of GDP for GTP, and GTPase-activating proteins (GAPs), which stimulate the hydrolysis of GTP to GDP (Ma et al., 2025). In its GTP-bound active form, KRAS undergoes a structural rearrangement that facilitates its interaction with downstream effectors, thereby activating key signaling pathways, making KRAS a central player in cellular signaling networks. KRAS cancer mutations disrupt cellular signaling pathways, leading to uncontrolled cell proliferation and survival. A complete GTPase reaction requires well-ordered conformations of the KRAS active site, which includes the phosphate-binding loop, P-loop (residues 10–17), switch I (residues 25–40) and switch II (residues 60–76) regions (Lu, Jang, Gu, et al., 2016; Lu, Jang, Nussinov, & Zhang, 2016; Vatansever et al., 2019) (Figure 1). KRAS can adopt both open and closed states in its active (GTP-bound) form, depending on the conformation of its switch regions (switch I and switch II). These states are dynamic and play a critical role in regulating KRAS signaling and interactions with effector proteins. In the GTP-bound state, switch I and switch II undergo conformational changes that are critical for effector protein binding. Historically, it has been assumed that the GTP-bound state predominantly adopts a "closed" conformation (state II), which is competent for effector binding and signaling (Baussand & Kleinjung, 2013). However, solution-state nuclear magnetic resonance spectroscopy (NMR) studies of human RAS (HRAS) bound to the non-hydrolyzable GTP analog, GMPPNP challenged this oversimplified view, demonstrating that even in the GTP-bound state, HRAS can sample two dominant conformational states in the switch I defined as state I (open conformation, incompatible with effector binding) and state II (closed conformation, facilitating high-affinity binding to effector proteins) exist in the dynamic equilibrium (Spoerner et al., 2001, 2005, 2010). These NMR studies demonstrated that the GTP-bound state of KRAS is not a single, static conformation but rather a dynamic ensemble of states, some of which are signaling-competent (closed) and others signaling-incompetent (open). A complex conformational dynamics in KRAS proteins and oncogenic mutants can modulate the interactions with their downstream effectors, including synchronized cross-talk motions between the effector and allosteric lobes (Chao et al., 2022). High-resolution structures of KRAS-GTP complexes have revealed that switch I can adopt multiple conformations (closed, open, and intermediate states) while maintaining GTP coordination and the Mg^{2+}–T35 interaction (Lu et al., 2018; Shima et al., 2010; Xu et al., 2017). In the open conformation, switch I is more flexible and less structured, making it incompatible with effector binding.

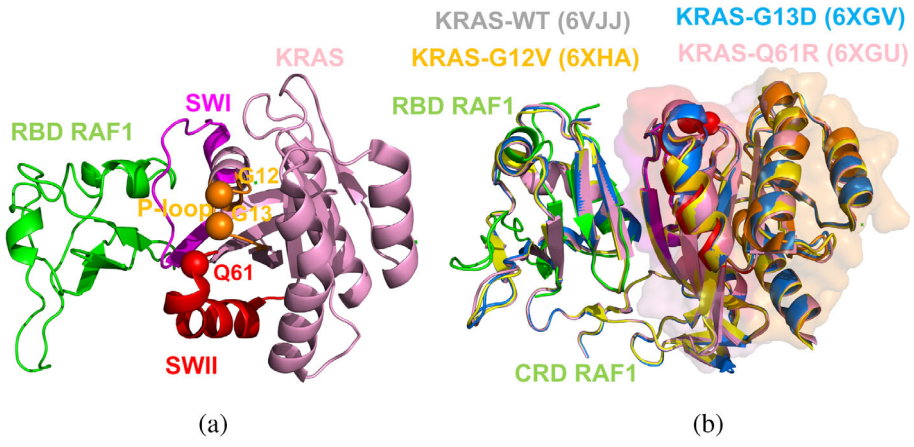

FIGURE 1 Structural overview and organization of the Kirsten rat sarcoma viral oncogene homolog (KRAS) protein with RAF1. (a) The crystal structure of wild-type (WT) KRAS (GMPPNP-bound) in complex with the RAS-binding domain (RBD) of RAF1/CRAF (PDB ID 6VJJ). The KRAS RBD is shown in pink ribbons and RAF1 is depicted in green ribbons. The functional KRAS regions are highlighted P-loop (residues 10–17 in orange ribbons), Switch I, SW1 (residues 24–40 in magenta ribbons), switch II, SWII (residues 60–76 in red ribbons). The sites of oncogenic mutants G12V, G13D (from P-loop are in orange), and Q61R (from SWII is in red) are shown in spheres colored according to the color of the respective KRAS functional region to which they belong. (b) Structural overlay of the crystal structure of WT KRAS (GMPPNP-bound) (in dark cyan ribbons) bound with the RBD of RAF1 (in green ribbons) (PDB ID 6VJJ); crystal structure of KRAS-G12V (in orange ribbons) with RBD-cysteine-rich domain (CRD) of RAF1 (PDB ID 6XHA); crystal structure of KRAS-G13D (in light blue ribbons) in complex with the RBD-CRD of RAF (PDB ID 6XGV); and the crystal structure of KRAS-Q61R (in pink ribbons) bound with RBD-CRD of RAF1 (PDB ID 6XGU). The sites of oncogenic mutants G12V, G13D, and Q61R are shown in red spheres.

The free-energy landscape of Ras-GTP complexes based on extensive explicit solvent simulations and supported by time-resolved fourier transform infrared (spectroscopy) experiments showed that the functional state 2 of Ras-GTP has two distinct substates that interconvert on the sub-microsecond scale in solution, pointing to a novel mechanism for Ras-GTP to selectively interact with GAPs and effectors (Li, Zhang, et al., 2018).

Most oncogenic mutations in RAS proteins, particularly at residues G12, G13, and Q61, disrupt normal GTPase activity by impairing the intrinsic GTP hydrolysis and/or interfering with GAP-mediated GTP hydrolysis. These mutations lock KRAS in its GTP-bound state, which is the biochemically defined active state of the protein (Huang et al., 2021). Oncogenic mutations can often exhibit context-dependent effects on binding affinity depending on post-translational modifications or interactions with regulatory proteins. For example, G12C stabilizes the GDP-bound state more than the GTP-bound state under certain conditions, requiring covalent inhibitors to target the GDP-bound form (Ostrem et al., 2013).

The prolonged activation induced by oncogenic mutations leads to constitutive downstream signaling through effectors driving oncogenic transformation. While oncogenic changes can induce relevant changes in the conformational dynamics of KRAS, it is critical to distinguish between the primary functional role of these mutations causing detrimental effects on catalytic function and thereby driving oncogenic behavior and the secondary effects of altered dynamics. Oncogenic mutations stabilize the active conformation while disrupting enzyme catalysis by altering the precise positioning of catalytic residues (Berta et al., 2023; Kolch et al., 2023). The impaired hydrolysis of GTP and the resulting stabilization of the active state are the root causes of oncogenic signaling. On the other hand, dynamic changes, such as enhanced flexibility in switch regions or stabilization of specific conformations, are likely downstream consequences of this dysfunction. Understanding the interplay between catalytic impairment and conformational dynamics is essential for elucidating how oncogenic mutations modulate KRAS activity. While this study focuses on the structural and dynamic consequences of these mutations, it is important to acknowledge that the observed changes in dynamics do not directly measure or establish the catalytic dysfunction caused by these mutations but rather provide complementary insights into their effects on protein interactions and effector binding.

KRAS has long been considered "undruggable" due to a lack of deep, well-defined binding pockets. However, recent advances in structural biology have identified cryptic allosteric pockets that can be targeted by small molecules. For example, sotorasib (AMG-510), a covalent inhibitor that targets the KRAS-G12C mutation, binds to a cryptic pocket outside the nucleotide-binding and effector-binding sites, locking KRAS-G12C in its inactive, GDP-bound state and preventing interaction with downstream effectors (Canon et al., 2019). Oncogenic mutations, including G12D, G12V, and Q61H, can differentially alter switch region conformations, disrupt the balance between open and closed states of KRAS and NRAS, impairing GTP hydrolysis and enhancing RAF affinity and signaling activity. NMR and hydrogen–deuterium exchange mass spectrometry (HDX-MS) examined switch I dynamics in the GTP state of KRAS, revealing co-existence of open state I and closed state II (Rennella et al., 2024). This study established the mechanism of action of a potent KRAS-G12D inhibitor, MRTX1133, targeting the switch II pocket and causing a complete shift of KRAS-G12D toward the "inactive" conformation. Structural and functional studies of KRAS-Q61H bound to GTP revealed that switch II allows for a more stable interaction with the switch I region (Zhou et al., 2020). NMR studies also delineated the differences in state I (inactive, effector binding deficient) and state II (active, effector binding enabled) present in several common KRAS oncogenic mutants (G12C, G12D, G12V, G13D, and Q61L) bound to its natural substrate GTP, showing that GTP-bound KRAS is primarily in state II conformation (Sharma et al., 2024). By integrating deep mutational scanning (DMS) with biological validation and structural analysis, a comprehensive structure–function analysis of KRAS variants showed that KRAS gain-of-function mutations at positions G12, G13, A59, K117, A146, and Q61 can lead to constitutive activation (Kwon et al., 2024). RAF1 binds KRAS through its RAS-binding domain (RBD) and cysteine-rich domain (CRD), where the switch I (residues 25–40) and switch II (residues 60–76) regions of KRAS emerged as key binding interface regions (Fetics et al., 2015; Tran et al., 2021). A pioneering experimental study of KRAS energetics and allostery combined structural biology and biophysical techniques to map the complete energetic and allosteric landscape of KRAS binding with several binding partners (Weng et al., 2024).

Despite the significant body of structural and biochemical studies of KRAS dynamics and binding, there are a number of questions including: (a) How do long-timescale conformational changes in KRAS, particularly in the switch regions, influence its binding to effector proteins? (b) What are allosteric networks that connect distal mutation sites (e.g., G12 and Q61) to the switch regions, and how do these networks modulate KRAS activity? (c) What are the structural and dynamic differences between various KRAS mutations (e.g., G12C, G12D, G12V, G13D, and Q61H) that lead to oncogenic outcomes? and (d) What are the thermodynamic drivers of binding hotspots to KRAS stability and allosteric effector binding?

Using an array of computational simulation approaches, the current study provides an integrated atomistic view of KRAS dynamics, energetics, and allosteric regulation, enabling a direct comparison and atomistic-level

rationalization of the latest experimental data on KRAS allostery and binding.

Computational studies elucidated many aspects of KRAS-RAF1 binding dynamics, energetics, and mechanisms. MD simulations showed that the switch I and switch II regions of KRAS are highly dynamic, influencing RAF1 binding (Chen et al., 2013). Multiscale MD simulations explored KRAS binding to RAF1 RBD-CRD domains, showing how membrane orientation affects protein dynamics (Vatansever et al., 2020). Atomistic MD simulations also detailed KRAS membrane binding, revealing differences in dynamics and interaction networks among KRAS-WT and oncogenic mutants (G12D, G12V, and G13D) (Li, Prakash, & Buck, 2018; Nguyen et al., 2022). Microsecond molecular dynamics (MD) simulations and free energy analysis uncovered distinct binding mechanisms and critical interaction hotspots for inhibitors trametinib and MRTX1133 targeting KRAS-G12D mutation (Ancy et al., 2024; Tu et al., 2024) revealing three KRAS binding pockets—the nucleotide-binding site, the switch-I/II pocket, and the allosteric switch-II/α3 pocket. Computer simulations of KRAS and oncogenic variants (G12C, G12D, G12V, and G13D) showed that G12C and G12D mutations stabilize the active state (Mir et al., 2024) while AMG-510 and MRTX1133 force these mutants into the inactive state (Pandey & Roy, 2025). Markov state models (MSM) analysis assessed KRAS-G12 mutant dynamics, revealing an allosteric hydrophobic signaling network and modulation of switch region dynamics manifested in multiple conformations, including intermediate states, during its GTPase cycle (Pantsar et al., 2018). Gaussian accelerated molecular dynamics (GaMD) combined with deep learning explored the effects of G12C mutations and effector protein binding on KRAS, demonstrating enhanced mobility in switch I and II regions (Chen, Wang, Yang, Zhao, & Hu, 2024). Multiple replica GaMD simulations examined the dynamic effect of Q61A, Q61H, and Q61L on the activity of KRAS, showing that these mutations can induce structural disorder of the switch I domain and disturb the activity of KRAS (Chen et al., 2022). It was also shown that phosphorylation at pY32, pY64, and pY137 positions on KRAS can promote transitions between closed and open states (Chen, Wang, Yang, Zhao, Zhao, & Hu, 2024) Overall, structural and computational studies showed that in its active state, KRAS predominantly adopts a stable closed conformation but can also transiently adopt open and intermediate states emerging during conformational fluctuations and induced by binding. The mechanisms underlying the balance between these states are complex and can be influenced by nucleotide binding, oncogenic mutations, and long-range effects induced by binding partners.

In this study, we employed microsecond MD simulations, MSM, computational mutational scanning, molecular mechanics generalized Born surface area (MM-GBSA) binding affinity calculations, and network modeling to simulate binding mechanisms of KRAS oncogenic mutants G12V, G13D, and Q61R in complexes with the RBD of RAF1. In addition, for structure-based mutational scanning, we also employed the crystal structures of KRAS-Q61R (GMPPNP-bound) and KRAS-G13D (GMPPNP-bound) in complex with the RBD and CRD of RAF1/CRAF. The current study reveals distinct conformational dynamics signatures of KRAS mutants G12V, G13D, and Q61R compared to wild-type (WT) KRAS, providing mechanistic insights into how specific mutations differentially modulate KRAS dynamics. Using MD-inferred conformational ensembles and dynamics-based network modeling, this study mapped potential allosteric hotspots and allosteric communication pathways in KRAS-RAF1 complexes. Consistent with the pioneering experimental analysis (Weng et al., 2024), our results show that the central β-sheet of KRAS acts as a hub for transmitting allosteric signals between distant functional sites, facilitating allosteric communication between the switch regions and the RAF1 binding interface. The study rigorously compares computational predictions with DMS experiments and structural studies. The predictions accurately reproduced the experimental data on allosteric binding hotspots located away from the KRAS-RAF1 interface in which mutations have strong effects on the binding free energy with RAF1 (Weng et al., 2024). Dynamic network analysis reveals critical allosteric centers and discovers a conserved allosteric architecture that can robustly mediate long-range interactions in the KRAS-RAF1 complexes and connect distant regions of KRAS, facilitating communication between the nucleotide-binding site and effector-binding site.

2 | MATERIALS AND METHODS

2.1 | Structural analysis and preparation of simulation systems

The crystal and cryogenic electron microscopy structures of the KRAS and KRAS complexes are obtained from the Protein Data Bank (PDB) (Rose et al., 2017). Multiple independent microsecond MD simulations are performed for the crystal structure of WT KRAS (GMPPNP-bound) in complex with the RBD of RAF1/CRAF (PDB ID 6VJJ); G12V KRAS mutant in the complex with the RBD of RAF1 (PDB ID 6VJJ); crystal structure of KRAS-G12V (GMPPNP-bound) in complex with the RBD and CRD of RAF1 (PDB ID 6XHA); crystal structure of KRAS-G13D (GMPPNP-bound) in complex with the RBD and CRD of RAF1 (PDB ID 6XGV); the crystal structure of KRAS-Q61R (GMPPNP-bound) in complex with RBD and CRD of RAF1 (PDB ID 6XGU). For simulated structures, hydrogen atoms and missing residues were initially modeled using the MODELER program (Webb & Sali, 2016) and subsequently reconstructed and optimized using the template-based loop prediction approach ArchPRED (Fernandez-Fuentes et al., 2006). The side chain rotamers were additionally optimized by the SCWRL4 tool (Krivov

et al., 2009). Protonation states of ionizable residues were assigned using PROPKA, ensuring histidine residues were in the appropriate tautomeric state (Olsson et al., 2011; Søndergaard et al., 2011). The tleap module in AMBER was used to generate the topology (prmtop) and coordinate (inpcrd) files (Salomon-Ferrer et al., 2012). The system was solvated in a TIP3P water box with a 12 Å buffer and neutralized using Na^+ or Cl^- ions. The final system was saved for further simulations. Molecular mechanics parameters of proteins were assigned according to the ff14SB force field (Maier et al., 2015; Tian et al., 2020). The protein structures were energy-minimized to remove steric clashes and optimize the structure.

2.2 | All-atom molecular dynamics simulations

The simulation systems were processed through several stages of structure preparation. First, two stages of minimization were performed: (a) with restraints on the protein backbone to relax solvent and ions, and (b) without restraints to minimize the entire system. The minimization was carried out using the pmemd.cuda module with the following parameters: 1000 cycles of steepest descent followed by 500 cycles of conjugate gradient minimization, a cutoff of 10 Å for non-bonded interactions, and the ff14SB force field for proteins (Maier et al., 2015; Tian et al., 2020). After minimization, the system is heated from 100 to 300 K over 1 ns of simulation time at a constant volume, with integration time 1 fs. Then we relax the system at a constant pressure with protein restraints over 1 ns of simulation time at a constant pressure with restraints set to 1 kcal/mol $Å^2$. Finally, we relax the system with no restraints for 1 ns of simulation time at a constant pressure. This is followed by 2 μs of production period with 20,000 frames saved for analysis. To ensure robust sampling of the conformational landscape, we performed multiple independent 2 μs MD simulations for each system. Each independent replica was simulated for 2 μs, and a total of three replicas were conducted for each system, resulting in an aggregate simulation time of 6 μs per system. Across all systems studied (KRAS-WT, G12V, G13D, and Q61R mutants in complex with RAF1), the total aggregate simulation time amounted to 24 μs. A detailed breakdown of the simulation times for each system is provided in Table S1. MD simulations were performed under isothermal-isobaric ensemble (NPT) conditions (300 K, 1 bar). The temperature was maintained using the Langevin thermostat, and pressure was controlled with the Monte Carlo barostat. A time step of 2 fs was used, and bonds involving hydrogen atoms were constrained using the SHarer's and Knight's equation (SHAKE) algorithm. MD trajectories were saved every 100 ps for analysis. The ff14SB force field was used for proteins, and the TIP3P model was used for water.

The CPPTRAJ software in AMBER 18 was used to calculate the root mean squared deviation (RMSD) and root mean squared fluctuation (RMSF) of MD simulation trajectories in which the initial structure was used as the reference (Roe & Cheatham III, 2013). The structures were visualized using Visual Molecular Dynamics (VMD 1.9.3) (Fernandes et al., 2019) and PyMOL (Schrodinger, LLC. 2010. The PyMOL Molecular Graphics System, Version 2.4.0, Schrödinger, LLC).

To identify the dynamical coupling of the motions between protein segments, the cross-correlation coefficient (C_{ij}) was proposed for measuring the motion correlation between the C_α atom pair in residues i and j, which is defined as

$$C_{ij} = \frac{\langle \Delta r_i \times \Delta r_j \rangle}{\left(\langle \Delta r_i^2 \rangle \langle \Delta r_j^2 \rangle \right)^{1/2}}, \quad (1)$$

where Δr_i and Δr_j are the displacements from the mean position of the C_α atom pair in residues i and j, respectively, that are evaluated over the sampled period. Positive C_{ij} are associated with correlated motion in the residue pair, whereas negative C_{ij} stands for negatively correlated motion. The cross-correlation analysis in this work was implemented using the Bio3D package (Grant et al., 2021).

2.3 | Markov state model

Stochastic MSMs (Bowman et al., 2015; Suárez et al., 2016; Wu et al., 2016) have become increasingly useful states-and-rates models with the mature and robust software infrastructure (Bowman, 2014; Bowman & Noé, 2014) for describing the transitions between functional protein states and modeling of allosteric events. In MSM, protein dynamics is modeled as a kinetic process consisting of a series of Markovian transitions between different conformational states at discrete time intervals. A specific time interval, referred to as lag time, needs to be determined to construct the transition matrix. First, the k-means clustering method is conducted on the projected low-dimensional space, and each simulation frame is assigned to a microstate. The transition counting is constructed based on a specific time interval lag time τ. Macrostates are kinetically clustered based on the Perron-cluster cluster analysis (PCCA++) (Trendelkamp-Schroer et al., 2015) and are considered to be kinetically separate equilibrium states. The transition matrix and transition probability were calculated to quantify the transition dynamics among macrostates. The corresponding transition probability from state i to state j is calculated as:

$$P_{ij}(\tau) = \text{Prob}\left(x_t + \tau \in S_j | x_t \in Si\right). \quad (2)$$

A proper lag time is required for MSM to be Markovian. The value of the lag time and the number of macrostates are selected based on the result of estimated relaxation timescale (Bowman et al., 2009). The implied timescales can be calculated using the eigenvalues (λ_i) in the transition matrix as

$$t_i = -\frac{\tau}{\ln|\lambda_i(\tau)|}. \quad (3)$$

The number of protein metastable states associated with these slow relaxation timescales can be inferred based on the convergence of implied relaxation timescale. These metastable states effectively discretize the conformational landscape. The MSM building was conducted using the PyEMMA package (v2.5.12) (Scherer et al., 2015). Based on the transition matrix, we obtain implied timescales for transitions between various regions of phase space and use this information to determine the number of metastable states. The number of metastable states also defines the resolution of the model by determining how large a barrier must be in order to divide phase space into multiple states.

2.4 | Mutational scanning and sensitivity analysis of the KRAS residues: quantifying effects of mutations on KRAS binding and protein stability

To comprehensively characterize the binding energetics and interface of KRAS complexes, we employed two complementary computational approaches: BeAtMuSiC and MM-GBSA. BeAtMuSiC, a knowledge-based statistical potential method, was used to identify binding affinity hotspot positions whose mutations significantly destabilize the complex. This approach provides a rapid and residue-level map of critical residues at the binding interface that contribute most to protein stability and binding affinity. These hotspots are essential for understanding the structural determinants of KRAS binding. MM-GBSA computations will be subsequently employed for rigorous binding affinity computations and decomposition of the binding free energy into its thermodynamic components, revealing the specific types of interactions that drive binding. This physics-based method elucidates the "thermodynamic drivers" of binding, offering mechanistic insights into how these interactions vary across different complexes. Together, these methods provide a hierarchical and comprehensive view of KRAS binding determinants. BeAtMuSiC identifies the "where" (which residues are critical), while MM-GBSA explains the "why" (what types of interactions drive binding).

We conducted a systematic mutational scanning analysis of the KRAS residues in the KRAS complexes using conformational ensembles of KRAS-RAF1 complexes and averaging of mutation-induced energy changes. Every KRAS residue was systematically mutated using all substitutions, and corresponding protein stability and binding free energy changes were computed with the knowledge-based BeAtMuSiC approach (Dehouck et al., 2006, 2009, 2013). This approach is based on statistical potentials describing the pairwise inter-residue distances, backbone torsion angles, and solvent accessibilities, and considers the effect of the mutation on the strength of the interactions at the interface and on the overall stability of the complex. The binding free energy of the protein–protein complex can be expressed as the difference in the free energy of the complex and free energy of the two protein binding partners:

$$\Delta G_{\text{bind}} = G^{\text{com}} - G^{\text{A}} - G^{\text{B}} \quad (4)$$

The change of the binding energy due to a mutation was calculated then as follows:

$$\Delta\Delta G_{\text{bind}} = \Delta G^{\text{mut}}_{\text{bind}} - \Delta G^{\text{wt}}_{\text{bind}}. \quad (5)$$

We leveraged rapid calculations based on statistical potentials to compute the ensemble-averaged binding free energy changes using equilibrium samples from simulation trajectories. The binding free energy changes were obtained by averaging the results over 1000 and 10,000 equilibrium samples for each of the systems studied.

2.5 | MM-GBSA binding free energy computations of KRAS-RAF1 complexes

We calculated the ensemble-averaged changes in binding free energy using 1000 equilibrium samples obtained from simulation trajectories for each system under study. The binding free energies of the KRJAS-RAF1 complexes were assessed using the MM-GBSA approach (Kollman et al., 2000; Srinivasan et al., 1998). The energy decomposition analysis evaluates the contribution of each amino acid to the binding of KRAS to the RAF1 protein (Hou et al., 2011; Weng, Wang, Wang, et al., 2019). The binding free energy for the KRAS-RAF1 complex was obtained using:

$$\Delta G_{\text{bind}} = G_{\text{KRAS-RAF1}} - G_{\text{KRAS}} - G_{\text{RAF1}}, \quad (6)$$

$$\Delta G_{\text{bind,MMGBSA}} = \Delta E_{\text{MM}} + \Delta G_{\text{sol}} - T\Delta S, \quad (7)$$

where ΔE_{MM} is total gas phase energy (sum of $\Delta E_{\text{internal}}$, $\Delta E_{\text{electrostatic}}$, and ΔE_{vdw}); ΔG_{sol} is the sum of

polar (ΔG_{GB}) and non-polar (ΔG_{SA}) contributions to solvation. Here, $G_{KRAS–RAF1}$ represents the average over the snapshots of a single-trajectory of the complex, G_{KRAS} and G_{RAF1} correspond to the free energy of KRAS and RAF1 protein, respectively. The polar and non-polar contributions to the solvation free energy are calculated using a Generalized Born solvent model and consideration of the solvent accessible surface area (Mongan et al., 2007). MM-GBSA is employed to predict the binding free energy and decompose the free energy contributions to the binding free energy of a protein–protein complex on a per-residue basis. The binding free energy with MM-GBSA was computed by averaging the results of computations over 1000 samples from the equilibrium ensembles. First, the computational protocol must be selected between the "single-trajectory" (one trajectory of the complex) or "separate-trajectory" (three separate trajectories of the complex, receptor, and ligand). To reduce the noise in the calculations, it is common that each term is evaluated on frames from the trajectory of the bound complex. In this study, we choose the "single-trajectory" protocol because it is less noisy due to the cancelation of intermolecular energy contributions. This protocol applies to cases where significant structural changes upon binding are not expected. Entropy calculations typically dominate the computational cost of the MM-GBSA estimates. Therefore, it may be calculated only for a subset of the snapshots, or this term can be omitted (Sun et al., 2018; Weng, Wang, Chen, et al., 2019). However, for the absolute affinities, the entropy term is needed, owing to the loss of translational and rotational freedom when the ligand binds. In this study, the entropy contribution was not included in the calculations of binding free energies of the complexes because the entropic differences in estimates of relative binding affinities are expected to be small owing to small mutational changes and preservation of the conformational dynamics (Sun et al., 2018; Weng, Wang, Chen, et al., 2019). MM-GBSA energies were evaluated with the MMPBSA.py script in the AmberTools21 package (Miller III et al., 2012).

2.6 | Graph-based dynamic network analysis of protein ensembles

To analyze protein structures, we employed a graph-based representation where residues are modeled as network nodes, and non-covalent interactions between residue side chains define the edges. The residue interaction networks were constructed by defining edges based on non-covalent interactions between residue side chains (Brinda & Vishveshwara, 2005; Vijayabaskar & Vishveshwara, 2010). The Residue Interaction Network Generator (RING) program (Clementel et al., 2022; Del Conte et al., 2024; Martin et al., 2011; Piovesan et al., 2016) was used to generate residue interaction networks from the conformational ensemble. The edges in these networks were weighted to reflect the frequency of interactions observed in the ensemble. Network graph calculations were performed using the Python package NetworkX (Floyd, 1962; Hagberg et al., 2008). This included the computation of key network parameters, such as shortest paths and betweenness centrality, to identify residues critical for communication within the protein structure. The short path betweenness (SPC) of residue *i* is defined to be the sum of the fraction of shortest paths between all pairs of residues that pass through residue *i*:

$$C_b(n_i) = \sum_{j<k}^{N} \frac{g_{jk}(i)}{g_{jk}}, \tag{8}$$

where g_{jk} denotes the number of shortest geodesics paths connecting j and k, and $g_{jk}(i)$ is the number of shortest paths between residues j and k passing through the node n_i. Residues with high occurrence in the shortest paths connecting all residue pairs have a higher betweenness values. For each node n, the betweenness value is normalized by the number of node pairs excluding n given as $(N-1)(N-2)/2$, where N is the total number of nodes in the connected component that node n belongs to. To account for differences in network size, the betweenness centrality of each residue ii was normalized by the number of node pairs excluding ii. The normalized SPC of residue i can be expressed as:

$$C_b(n_i) = \frac{1}{(N-1)(N-2)} \sum_{\substack{j<k \\ j \neq i \neq k}}^{N} \frac{g_{jk}(i)}{g_{jk}}, \tag{9}$$

g_{jk} is the number of shortest paths between residues j and k; $g_{jk}(i)$ is the fraction of these shortest paths that pass through residue i.

2.7 | Network-based mutational profiling of allosteric residue centrality

Through mutation-based perturbations of protein residues, we compute dynamic couplings of residues and changes in the SPC centrality averaged over all possible modifications in a given position. The change of SPC upon mutational changes of each node is reminiscent of the calculation of residue centralities by systematically removing nodes from the network.

$$\Delta L_i = \left\langle \left|\left| \Delta L_i^{\text{node}}(j) \right|\right|^2 \right\rangle, \tag{10}$$

where i is a given site, j is a mutation and $\langle \cdots \rangle$ denotes averaging over mutations. $\Delta L_i^{\text{node}}(j)$ describes the

change of SPC parameters upon mutation *j* in a residue node *i*. ΔL_i is the average change of average short path length triggered by mutational changes in position *i*.

Z-score is then calculated for each node as follows:

$$Z_i = \frac{\Delta L_i - \langle \Delta L \rangle}{\sigma}. \quad (11)$$

$\langle \Delta L \rangle$ is the change of the SPC network parameter under mutational scanning averaged over all protein residues and σ is the corresponding standard deviation. The ensemble-average *Z*-score changes are computed from network analysis of the conformational ensembles of KRAS-RAF1 complexes using 1000 snapshots of the simulation trajectory. Through this approach, we evaluate the effect of mutations in the KRAS residues on allosteric communications with RAF1.

3 | RESULTS

3.1 | MD simulations of the KRAS-WT, G12V, G13D, and Q61R complexes reveal distinct dynamic signatures of RBD proteins

Multiple independent microsecond simulations were performed for the KRAS-WT complex with the RBD of RAF1 (PDB ID 6VJJ), KRAS-G12V in complex with RAF1 (RBD-CRD) (PDB ID 6XHA), KRAS-G13D in complex with RAF1(RBD-CRD) (PDB ID 6XGV), and KRAS-Q61R in complex with RAF1 (RBD-CRD) (PDB ID 6XGU) (Tran et al., 2021) providing a detailed account of the dynamic behavior, stability, and interactions (Figure 1). Structural studies of G12V, G13D, and Q61R mutants of KRAS complexed with RAF1(RBD-CRD) showed high similarity for all three mutants and virtually identical interaction interfaces and switch conformations (Tran et al., 2021), suggesting that the RBDs of RAF1 bind to oncogenic KRAS mutants similarly to KRAS-WT (Figure 1). MD simulations are initiated from the closed conformation of switch I (state II) in which the active site Mg^{2+} is coordinated by the β- and γ-phosphates of GTP and the side chains of switch I residues S17 and T35, with the side chain of Y32 located over the nucleotide (Figure 1).

We performed a structural superposition of the KRAS-WT complex with RBD RAF1 and the three KRAS mutant complexes (G12V, G13D, and Q61R). The RMSD values for C_α atoms between WT KRAS and each mutant ranged from 0.8 to 1.2 Å, indicating minimal conformational differences in the overall architecture of the complexes (Figure 1b). This minimizes structural heterogeneity and ensures that observed differences are not artifacts of varying experimental setups.

The conformational flexibility of the KRAS and RAF1 was analyzed by calculating the RMSDs (Figures S1 and S2) and the root mean square fluctuations (RMSF) distribution for the KRAS residues in different complexes (Figure 2). The RMSD profiles for the KRAS residues demonstrated consistent convergence of the MD trajectories for the KRAS-WT complex for all three trajectories, reaching a stable equilibrium state after approximately 500 ns (Figure S1A). A synchronous behavior was seen for three independent microsecond MD trajectories for KRAS-G12V, where full convergence is typically reached after 800 ns to 1 μs (Figure S1B). Some divergence in RMSD profiles was observed for the MD trajectories of the KRAS-G13D complex (Figure S1C), reflecting a more heterogeneous ensemble of KRAS conformations in this variant. For the KRAS-Q61R complex, the RMSD profiles also showed moderate heterogeneity among three microsecond trajectories, stabilizing after ∼500 to 700 ns (Figure S1D). The RMSDs for RAF1 displayed minor variability across trajectories for the KRAS-WT, G13D, and Q61R variants, highlighting the functionally significant plasticity of both binding partners in the KRAS-RAF1 complexes (Figure S2). The RMSF profiles revealed that the KRAS-WT complex with RBD RAF1 became stable on the microsecond simulation timescale, with the RBD of RAF1 maintaining its binding to the switch I and switch II regions of KRAS (Figure 2a). These regions are critical for GTP binding, effector interaction, and downstream signaling. The P-loop is a highly conserved region in KRAS that interacts with the phosphate groups of GTP. It plays a critical role in nucleotide binding and stabilization. MD simulations showed that the P-loop (residues 10–17) exhibits moderate flexibility that allows the P-loop to adapt to the binding of GTP and accommodate conformational changes during the GTPase cycle (Figure 2a).

The switch I region displayed some flexibility, particularly evident in some of the independent microsecond simulations, fluctuating between semi-open (inactive) states and a dominant ensemble of ordered, closed (active) states (Figure 2a). Notably, however, the population is dominated by the fully ordered closed conformations (Figure 2a). The prevalent conformation of switch I is the fully active state that is stabilized by GTP binding and enables high-affinity binding to the RBD of RAF1. The critical residues in the switch I region, such as Y32, D33, and E37 interact with the RBD of RAF1 in the active state (Figure 2a) where particularly D33 forms a salt bridge with R59 in the RBD and E37 interacts with R67 in the RBD. A small fraction of the detected semi-open conformations is likely intermediate states of switch I.

The G12V mutation in KRAS is one of the most common oncogenic mutations and has effects on the structure, dynamics, and function of KRAS, particularly in its interaction with the downstream effector RAF1. Recent studies suggested that G12V can have a subtle impact on the conformation of switch I and surprisingly

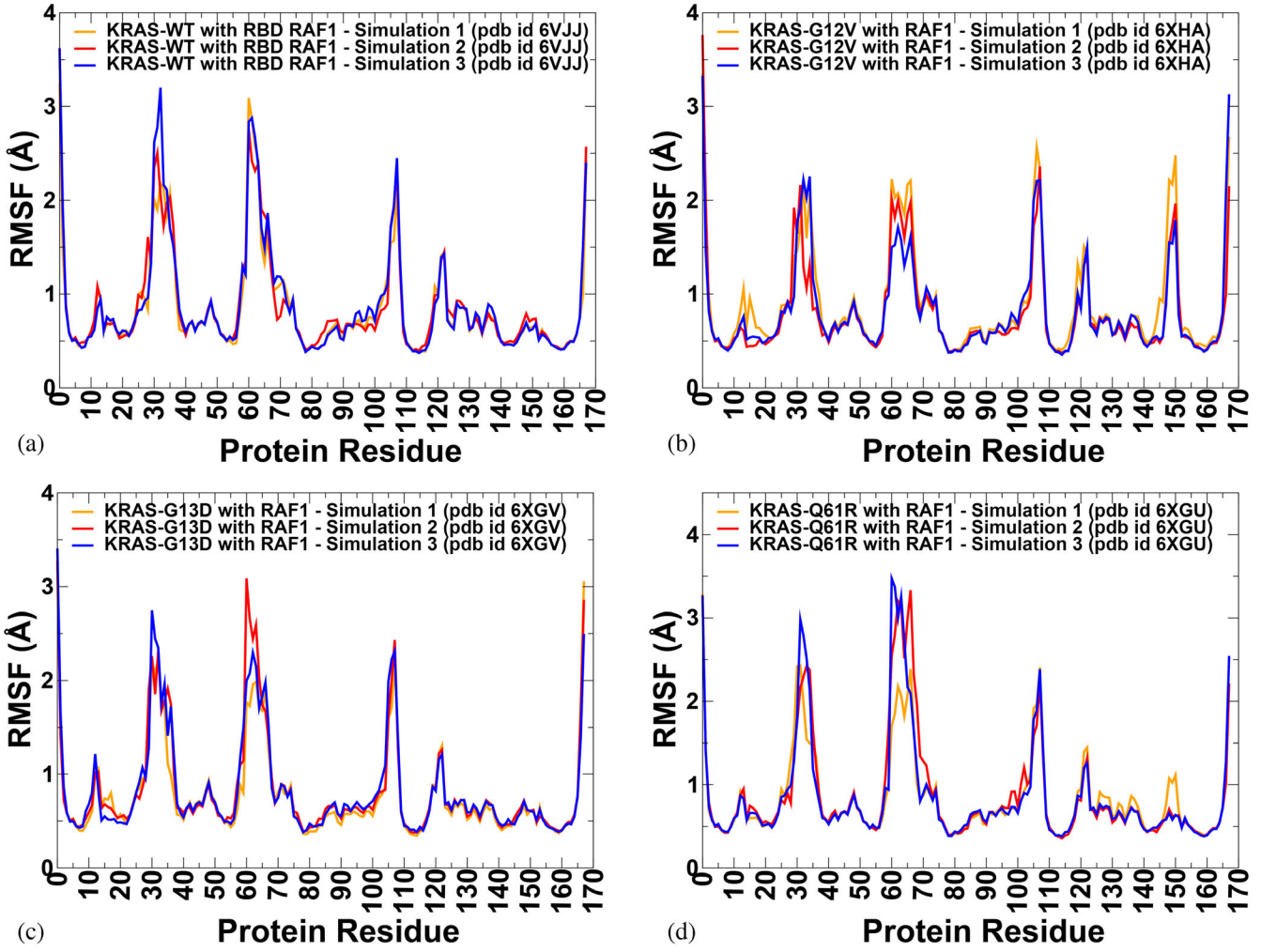

FIGURE 2 Conformational dynamics profiles of the Kirsten rat sarcoma viral oncogene homolog (KRAS) protein residues obtained from three independent molecular dynamics (MD) simulations of the KRAS complexes with RAF1. (a) The root mean squared fluctuation (RMSF) profiles for the RAS-binding domain (RBD) residues from three independent 2 μs MD simulations of the crystal structure of wild-type (WT) KRAS (GMPPNP-bound) bound with the RBD of RAF1 (PDB ID 6VJJ); (b) KRAS-G12V mutant bound with RAF1 (PDB ID 6XHA); (c) KRAS-G13D bound with RAF1 (PDB ID 6XGV) (d) KRAS-Q61R bound with RAF1/CRAF (PDB ID 6XGU). The conformational dynamic profiles are shown in orange lines (simulation 1), red lines (simulation 2), and blue lines (simulation 3).

tend to shift the populations toward an inactive state (Rennella et al., 2024). Conformational dynamics profiles for the KRAS-G12V complex with RAF1 indicated that the G12V mutation can reduce the flexibility of the switch I and II regions thus stabilizing the active conformation. This observation can be explained by considering the specific structural and dynamic effects of the G12V mutation (Figure 2b). The switch I region is directly connected to the P-loop and is sensitive to changes in the nucleotide-binding site (Figure 1). According to our results, the G12V mutation may restrict the flexibility of the switch I region by stabilizing its interactions with GTP and the P-loop (Figure 2b). The switch II region is also influenced by the P-loop and the nucleotide-binding site. The G12V mutation may reduce switch II fluctuations by stabilizing the overall active conformation of KRAS, including the orientation of switch II relative to switch I and the nucleotide. This stabilization may reduce the conformational entropy of the switch regions by favoring a specific state favorable for RAF1 effector binding over a dynamic ensemble of states (Figure 2b). Through these dynamic changes, the oncogenic G12V mutation may promote prolonged effector binding contributing to oncogenic transformation. In addition, the reduced flexibility of switch I limits its ability to adopt alternative conformations, which may affect its interaction with other regulatory proteins.

G13D is another critical residue that can be mutated in cancer. We employed the crystal structure of KRAS-G13D (GMPPNP-bound) in complex with the RBD and CRD of RAF1 (PDB ID 6XGV) and also the KRAS-G13D modeled mutant based on the crystal structure of the KRAS-WT bound to RAF1 (PDB ID 6VJJ). MD simulations showed that the G13D mutation in KRAS

moderately reduces fluctuations in the switch I region while moderately increasing the flexibility of the switch II region as seen in the KRAS-WT (Figure 2c). Our results suggested that the G13D mutation may moderately reduce switch I fluctuations due to stabilization of the P-loop through electrostatic interactions with the K117 residue. These results are consistent with structural studies revealing that the switch regions of KRAS show minor conformational changes in the structures of oncogenic mutants G13D complexed with RBD-CRD when compared with the KRAS-WT structure (Ostrem et al., 2013). Interestingly, the RMSF profiles (Figure 2c) indicated that the mobility of the switch II region may be restored back to the KRAS-WT level. The observed functional differences among various oncogenic mutants are likely rooted in subtle conformational and dynamic differences. Similar to the NMR studies (Chao et al., 2023) we observed that the D13 side chain can sample several rotameric conformations and interact with the positively charged K117 in the allosteric lobe (residues 87–166) of KRAS, thus stabilizing the switch I required for productive binding with the effector protein. Our results showed that KRAS-G13D adopts a stable conformation of switch I while allowing functionally relevant variability in switch II (Figure 2c). The increased flexibility of switch II facilitates its interaction with the RBD of RAF1, as the region can more easily adopt the active conformation required for binding. It may also enhance the dynamic allosteric communication between switch I and switch II. The increased flexibility of switch II allows it to interact more dynamically with switch I, promoting a more cooperative interaction. Our results are consistent with other computational studies (Vatansever et al., 2020) that indicated that the ability of oncogenic mutations on the P-loop G12C, G12V, and G13D can increase the flexibility of the switch II region.

The Q61R mutation stabilizes the active conformation of switch I by inducing conformational changes in the switch II region, which are propagated to switch I (Figure 2d). The RMSF profiles for the KRAS-Q61R mutant showed the increased variability of switch II, while the thermal fluctuations of the open configuration of switch I are suppressed (Figure 2d). Hence, MD simulations of Q61R-mutated KRAS revealed the increased flexibility in the switch II region and the reduced flexibility in the switch I region. The stabilized closed conformation of switch I assures the fidelity of its interaction with the RBD of RAF1. A similar pattern was found for the G13D mutant, but the variability of switch II becomes more pronounced for the Q61R mutant.

The divergence in the RMSD profiles and variations in the RMSFs observed for G13D, along with moderate heterogeneity seen for Q61R, highlight noticeable differences in the dynamic behavior of these mutants compared to the more rigid G12V mutant. These differences could have implications for understanding the functional mechanisms. The broader ensemble of conformations sampled by G13D suggests increased flexibility in certain regions (e.g., switch II), enabling it to adopt diverse functional states. This flexibility may facilitate interactions with a wider range of effectors or regulators, contributing to its oncogenic activity. The moderate heterogeneity in RMSD profiles for Q61R reflects its unique ability to stabilize the active state while introducing variability in switch II dynamics. This mutant exhibits reduced flexibility in switch I, which is critical for effector binding, but increased variability in switch II, which could modulate allosteric communication. The expanded conformational landscape of Q61R may present opportunities for targeting cryptic pockets that are transiently accessible. It is important to caution that the observed heterogeneity in conformational dynamics may partly reflect conformational sampling effects and does not directly compensate for the impaired catalytic function caused by these mutations. Instead, these dynamic changes are supporting effects that modulate the interaction networks and enable efficient signaling output of KRAS. While the flexibility of G13D and Q61R may expose transiently accessible pockets for potential inhibitors, any conclusions about druggability must be considered in the context of the primary catalytic dysfunction.

RBD RAF1 is a structurally dynamic domain composed of a four-stranded antiparallel β-sheet (residues 56–63, 66–73, 96–101, and 125–130) and a single α-helix (residues 74–89). The core of the RBD composed of a β-sheet and α-helix structure remains highly stable throughout the interaction with KRAS (Figure 1). The flexible loops (residues 51–55 and 84–88) allow the RBD to adapt to the conformational changes in KRAS during binding. The moderate flexibility of the RBD loops, combined with the stability of its core structure, allows the RBD to effectively interact with the flexible switch regions of KRAS (Figure S3). The recent NMR experiments showed that Q61R leads to a complete shift toward the active state and behaves differently from the other oncogenic mutations at G12 and G13 positions (Rennella et al., 2024). Our simulations observed a stable hydrogen bond between the Q61R side chain and the T35 backbone carbonyl oxygen that stabilizes switch I residues P34, T35, and I36. These results corroborate with these experiments, suggesting that the balance between the rigidification of switch I and the flexibility of switch II can promote a shift toward the active state compatible with RAF1 binding (Rennella et al., 2024). The stable switch I conformation enhances the interaction with the RBD of RAF1, which may have functional implications for prolonged signaling. These differences highlight mutation-specific effects on the dynamic behavior of switch I and switch II regions, with notable implications for KRAS signaling and effector interactions.

MD simulations of KRAS-WT revealed that switch I can adopt multiple conformations (stable closed and

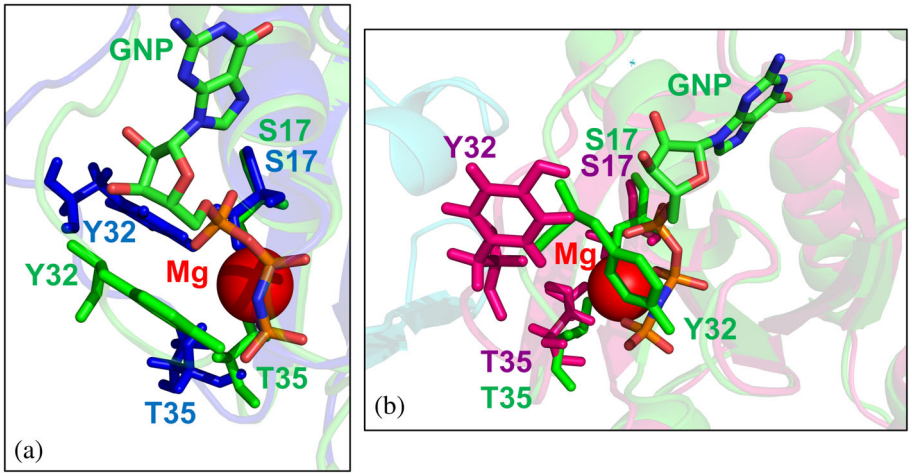

FIGURE 3 Structural maps of the conformational variations in the binding interactions for the Kirsten rat sarcoma viral oncogene homolog-wild-type (KRAS-WT) complex with RAS-binding domain RAF1. The two characteristic intermediate conformations of switch I are presented together with the dominant closed active conformations (state II). (a) One of the intermediate switch I conformations with S17, Y32, and T35 residues shown in blue sticks. Both T35 and Y32 are partly displaced from their optimal active positions. (b) Another intermediate conformation of switch I with Y32 pointing away from the nucleotide. S17, Y32, and T35 are shown in dark blue sticks. The residues in the fully active switch I conformation are shown in green sticks on panels (a) and (b).

intermediate states) while maintaining GTP coordination and the Mg^{2+}–T35 interaction. The prevalent conformation of switch I is the fully active state that is stabilized by GTP binding and enables high-affinity binding to the RBD of RAF1 (Figure 3). However, in addition, MD sampling of the conformational ensemble also detected various intermediate states of switch I in which this region is more flexible. We particularly characterized some of these conformations by highlighting the positions and interactions of key residues S17, Y32, and T35 with respect to Mg^{2+} and GNP (Figure 3). It can be seen that in the prevalent closed stable conformation of switch I (state II) of the active complex, T35 interacts with γ phosphate and Mg^{2+} while Y32 is closing over the nucleotide (Figure 3).

The highlighted two short-lived intermediate conformations observed during MD sampling of the active complex are characterized by partial loss of T35 contacts with Mg^{2+} and displacement of Y32 away from the state I form (Figure 3a). In one of these intermediate states, we observed Y32 pointing away from the nucleotide while both T35 and S17 maintained favorable contacts with Mg^{2+} (Figure 3b). Both of these intermediate sampled conformations could be classified as "semi-closed" suggesting that switch I is quite dynamic in the KRAS-WT bound with RBD RAF1 and could sample multiple states within the active complex. Only rarely observed short-lived samples were characteristic of more open switch I conformations (state I) in which both T35 and Y32 are positioned away from the nucleotide and T35 does not interact with Mg^{2+} ion.

Structural mapping of MD snapshots for the KRAS-WT (Figure 4a) and KRAS-G12V mutant complexes with RAF1 (Figure 4b) highlighted long-range dynamic changes induced by oncogenic mutation in the P-loop. In particular, structural projection of representative conformations from MD trajectories illustrated subtle and yet noticeably reduced thermal fluctuations, especially in the switch II region of the G12V mutant as compared to the KRAS-WT. Our results also suggest that the G12V mutation can affect the allosteric communication between switch I and switch II. The stabilized conformation of switch II reduces its ability to interact dynamically with switch I, leading to a more rigid and less cooperative interaction. This mutation seems to indirectly reduce the flexibility of switch I, as the stabilized switch II region limits the conformational changes that can propagate to switch I. As a result, the reduced flexibility and altered interactions between switch I and switch II may limit the ability of KRAS to adopt alternative conformations, which may affect its interaction with other regulatory proteins.

Our results showed that KRAS-G13D adopts a stable open conformation of switch I while allowing functionally relevant variability in switch II (Figure 4c). The increased flexibility of switch II facilitates its interaction with the RBD of RAF1, as the region can more easily adopt the active conformation required for binding. It may also enhance the dynamic allosteric communication between switch I and switch II.

To quantify dynamic couplings and correlations between motions of the KRAS regions, we performed the dynamic cross-correlation (DCC) residue analysis and reported the DCC maps for the KRAS-RAF1 complexes (Figure 5). By comparing the DCC maps of KRAS-WT and its oncogenic mutants (G12V, G13D, and Q61R), we can gain some insights into how mutations alter the dynamic couplings and correlations

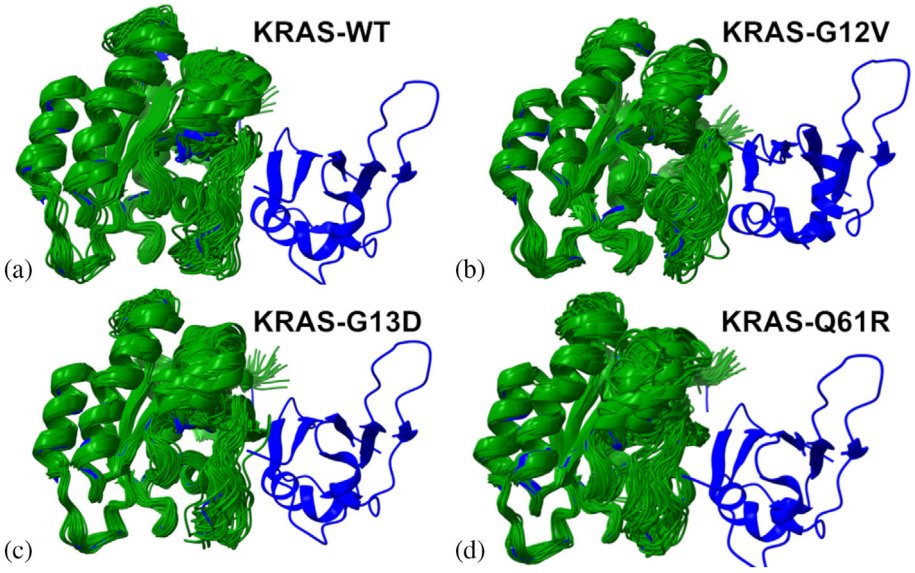

FIGURE 4 Structural mapping of the molecular dynamics (MD) snapshots taken each 100 ns three independent 2 μs MD simulations of the crystal structure of wild-type (WT) Kirsten rat sarcoma viral oncogene homolog (KRAS) (GMPPNP-bound) in complex with the RAS-binding domain (RBD) of RAF1/CRAF (PDB ID 6VJJ); (a), KRAS-G12V mutant in the complex with the RBD of RAF1/CRAF (PDB ID 6VJJ); (b), crystal structure of KRAS-G13D (GMPPNP-bound) in complex with the RBD and cysteine-rich domain (CRD) of RAF1/CRAF (PDB ID 6XGV) (c) and the crystal structure of KRAS-Q61R (GMPPNP-bound) in complex with RBD and CRD of RAF1/CRAF (PDB ID 6XGU) (d). The KRAS conformational samples are shown in dark green ribbons and overlayed over the crystal structure of the KRAS-WT complex with RBD RAF1 (shown in blue ribbons).

between motions of different KRAS regions. We observed KRAS-WT generally positive correlations between the P-loop (residues 10–17), Switch I (residues 25–40) and Switch II regions (residues 60–76) reflecting their functional coupling during nucleotide binding and hydrolysis (Figure 5a). The α-helices (α-helix 1: 15–24; α-helix 2: 67–73; α-helix 3: 87–104; α-helix 4: 127–136; α-helix 5: 148–166) and β-sheets (β-strand 1: 3–9; β-strand 2: 38–44; β-strand 5: 109–115; β-strand 6: 139–143) showed moderate correlations with the switch regions, and correlated motions are also observed between β-sheets (β-strand 3: 51–57; β-strand 4: 77–84) and the allosteric lobe (residues 87–166) of KRAS (Figure 6a).

The G12V mutation introduces a bulky hydrophobic residue in the P-loop. The reduced flexibility of switch II in the KRAS-G12V results in stronger positive correlations between residues within switch II as the region becomes more rigid. The stabilization of switch II reduces its correlations with other regions, such as the P-loop and switch I, as well as suppresses negative correlations between switch II and β-sheets (β-strand 3: 51–57; β-strand 4: 77–84) as the rigid switch II becomes less responsive to motions in these regions (Figure 5b).

DCC measures the correlation between the motions of pairs of residues over the course of MD simulation. Positive correlations indicate that residues move in the same direction, while negative correlations indicate anti-correlated motions.

The DCC map for KRAS-G13D featured the increased positive correlations within switch II residues (Figure 5c) and a stronger pattern of anti-correlated couplings between dynamic switch II and other regions, including the allosteric lobe of KRAS. The increased flexibility of switch II facilitates dynamic allosteric communication with switch I and promotes a more cooperative interaction. Although DCC maps for G13D (Figure 5c) and Q61R KRAS mutants (Figure 5d) look quite similar, there are some subtle dynamic differences. In particular, the increased mobility of switch II in the Q61R mutant can reduce positive correlations between switch I and switch II, reflecting the weakened dynamic coupling between these regions. In addition, a more stable switch I conformation is constrained through a transient hydrogen bond between the R61 side chain and the T35 backbone carbonyl oxygen. As a result, we observed weakened anti-correlated dynamic couplings between switch I and other regions (Figure 5d). The rigidification of switch I and a reduced dynamic coupling with switch I is a consequence of a shift toward the active state, which is compatible with RAF1 binding and prolonged signaling.

We also characterized essential motions and determined the hinge regions in the KRAS complexes (Figure 6) using principal component analysis (PCA) of trajectories using the CARMA package (Koukos & Glykos, 2013). The local minima along these profiles are typically aligned with the immobilized in global motions hinge centers, while the maxima correspond to

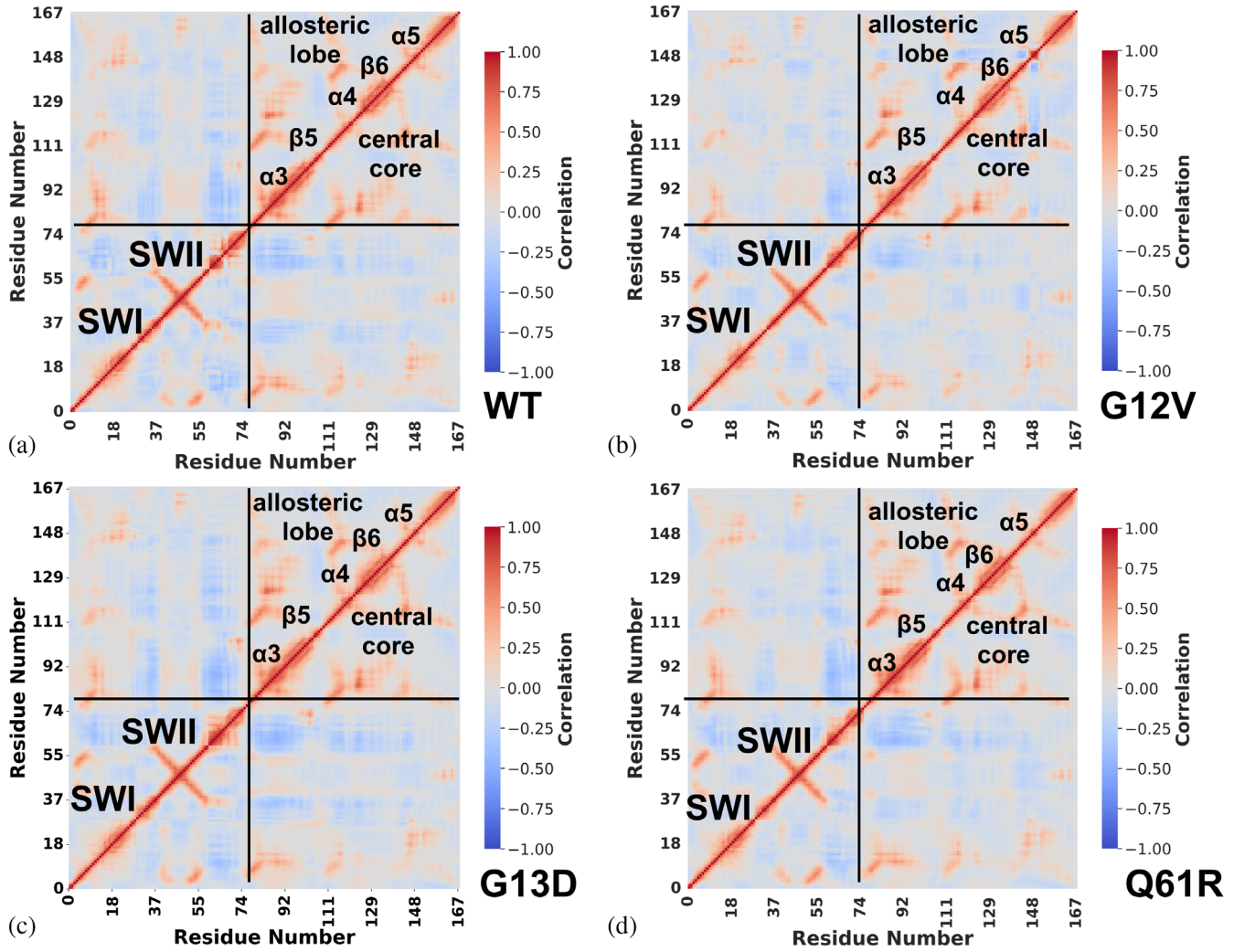

FIGURE 5 The dynamic cross-correlation maps for the Kirsten rat sarcoma viral oncogene homolog (KRAS) residues in the KRAS-wild-type (WT) complex with the RAS-binding domain (RBD) of RAF1/CRAF (PDB ID 6VJJ); (a) KRAS-G12V mutant complex with the RBD of RAF1/CRAF (PDB ID 6VJJ); (b) KRAS-G13D complex with the RBD and cysteine-rich domain (CRD) of RAF1/CRAF (PDB ID 6XGV) (c) and KRAS-Q61R complex with RBD and CRD of RAF1/CRAF (PDB ID 6XGU) (d).

the moving regions undergoing concerted movements leading to global changes in structure (Chao et al., 2023; Hagberg et al., 2008). The low-frequency "soft modes" are characterized by their cooperativity and there is a strong relationship between conformational changes and the "soft" modes of motions intrinsically accessible to protein structures (Haliloglu & Bahar, 2015; Zhang et al., 2020).

PCA analysis of slow mode profiles for KRAS complexes showed generally similar shapes reflecting significant structural and dynamic signatures shared by WT and mutants (Figure 6). First, we noticed that switch I (residues 24–40) and switch II (residues 60–76) are associated with the profile peaks, but the magnitude of functional displacements differs appreciably between KRAS-WT and mutants (Figure 6a). In addition, α-helix 4 (127–136) is also subjected to functional movements while the central core of the KRAS, including β-strand 4 (residues 77–84) and β-strand 5 (residues 109–115) are largely immobilized in slow mode motions, which is critical for maintaining the protein stability (Figure 6a). Importantly, among hinge points of the KRAS complexes that correspond to the major local minima of the profiles are critical binding sites E37, D38, S39, Y40, and R41 that anchor functional motions of switch I region (Figure 6a). The important finding of the slow mode analysis is the progressively decreasing amplitude of the major peak associated with displacements of switch I. Indeed, it can be noticed that the largest displacement of switch I is observed in the KRAS-WT complex, while smaller movements are seen in mutants, with KRAS-Q61 mutant displaying only very minor motions (Figure 6).

This pattern reflects a pattern of conformational dynamics changes in which switch I may sample not only active closed state II conformations but also more

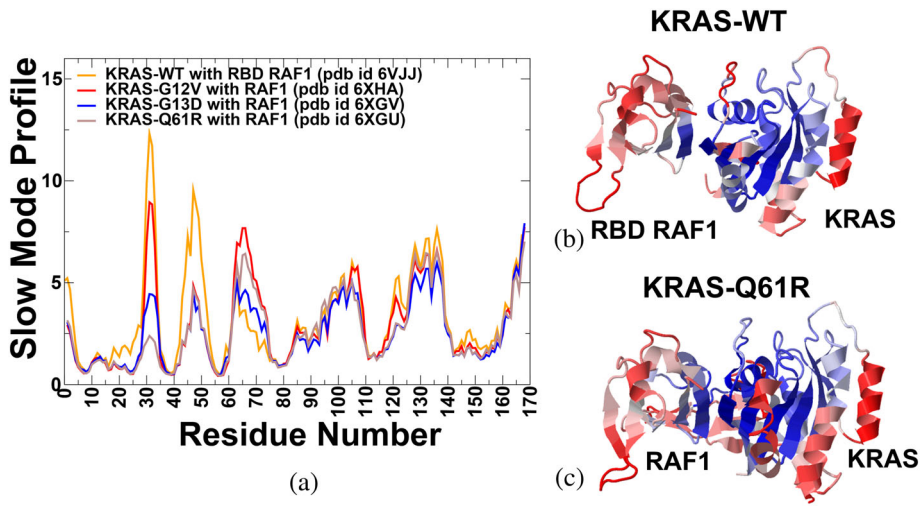

FIGURE 6 Functional dynamics and slow mode profiles of the Kirsten rat sarcoma viral oncogene homolog (KRAS) complexes. The essential mobility profiles are averaged over the first 10 lowest frequency modes. (a) The essential mobility/slow mode profiles of KRAS-wild-type (WT) bound with RAS-binding domain (RBD) RAF1 (in orange), KRAS-G12V (in red), KRAS-G13D (in blue) and KRAS-Q61R (in brown). (b) Structural mapping of slow mode profiles of KRAS-WT on the structure of KRAS-WT bound to RBD RAF1. (c) Structural mapping of slow mode profiles of KRAS-Q61R on the structure of KRAS-Q61 bound to RAF1. The structures are shown in ribbons with the rigidity-to-flexibility scale colored from blue to red with the most immobilized in functional motions regions in blue and most flexible in red.

flexible intermediate states. In contrast, we observed that movements of the switch I conformations are considerably rigidified in KRAS-Q61R that favors only closed active state II (Figure 6a). The stabilized closed conformation of switch I assures the fidelity of its interaction with the RBD of RAF1. Consistent with conformational dynamics results, a similar pattern is seen for the G13D mutant, but the rigidity of state II becomes more pronounced for the Q61R mutant. These results are consistent with the notion that the Q61R oncogenic mutation shifts the equilibrium fully toward the active closed state II and correspondingly binding to RAF can further strengthen the active state.

3.2 | Markov state modeling of KRAS conformational ensembles

While the analysis of MD simulations and functional movements provided important insights into the underlying conformational landscape, the high dimensionality of the data sets produced by simulations often hides salient dynamic signatures associated with the mechanisms of allosteric transitions. Here, to facilitate the conformational landscape analysis, we employed a dimensionality reduction method to project the results of MD simulations into low-dimensional space (Naritomi & Fuchigami, 2011; Schwantes & Pande, 2013; Sultan & Pande, 2017; Trozzi et al., 2021). Given a time-series of molecular coordinates provided by the MD trajectories, time-lagged independent component analysis (t-ICA) aims to reduce the dimensionality of the trajectories and to identify hidden key structural changes.

We leveraged conformational ensembles obtained from MD simulations for MSM analysis to estimate probabilities for protein transition among different macrostates. To build MSM, the dimensionality reduction process needs to retain information about how proteins transition among macrostates. We analyzed the relaxation timescales in MSM, also referred to as implied timescales. The relaxation timescale can be interpreted as the time needed for a system to change its state. To cluster different conformations into metastable states, the *k*-means clustering method was used to build clusters with the mean RMSD within the cluster smaller than 1 Å. In the t-ICA reduced 2D space, the *k*-means clustering method was applied to partition the 2D data. The top timescales are shown (Figure S4A). The trend of implied relaxation timescale revealed that the estimated timescale converged after approximately 10 ns, which was chosen as the lag time in the construction of MSM. The density plot revealed that several macrostates (macrostate 1, 2, and 5) are dominant and correspond to 28.49%, 42.05%, and 17.78% of the entire population of states obtained from MD simulations (Figure S4B). Interestingly, the low-dimensional projection of conformations showed that macrostates 1 and 5 occupy different "legs" of the distribution and may reflect different conformational signatures associated with semi-open and open KRAS conformations. The low-dimensional map of the KRAS-WT and KRAS mutant complexes highlighted a more restricted conformational space afforded by KRAS-G12V and KRAS-G13D mutants that appear to lock switch I in the active conformation, while a larger and more diverse conformational landscape is induced by the Q61R mutation

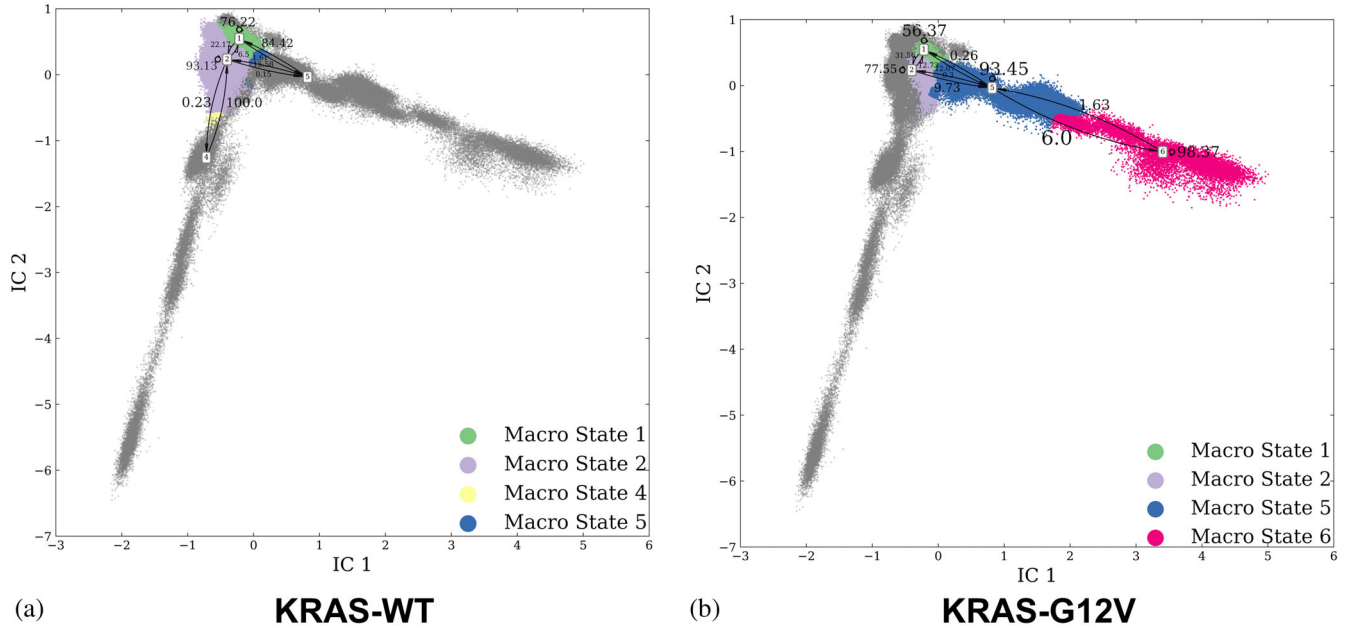

FIGURE 7 Markov state models analysis of the conformational landscape for the Kirsten rat sarcoma viral oncogene homolog-wild-type (KRAS-WT) complex, KRAS-G12V complexes. The transition probability maps among different macrostates with the 10 ns lag time for the KRAS-WT complex (a), KRAS-G12V (b). The high percentage of self-conservation probability shows the stability of macrostates.

that exerts activation through different dynamic mechanisms and redistribution of the conformational landscape (Figure S5). The hexagon binning was employed to represent the distribution density of all MD simulations, with each hexagon representing a small region, and the color bar showing the frequency of this region (Figure S5). Since differences in the conformational space of KRAS are localized to the switch I region corresponding to the closed and semi-open forms, we infer that the distinct signatures of major macrostates may indeed reflect this principal pattern of KRAS dynamics.

After the partition of the MSM macrostates was determined, the stationary distribution and transition probabilities were calculated based on the constructed MSM (Figures 7 and 8). The transition probabilities are determined among different macrostates. The high percentage of self-conservation probability shows the stability of macrostates. MSM identifies a dominant macrostate 2 (93%) corresponding to the fully active conformation of KRAS-WT, where both switch I and switch II are ordered and engaged with the RBD of RAF1 (Figure 7a). In addition, the KRAS-WT populates macrostates 1, 4, and 5. For KRAS-G12V, the distribution of macrostates is similar, with dominant microstate 2 (77%) and macrostates 1, 5, and 6 that occupy only one "leg" of the distribution (Figure 7b). These macrostates reflect semi-open transient conformations that KRAS-WT samples during the transition between the active and inactive states of switch I.

MSM analysis of KRAS-G13D demonstrated an even narrower range of transitions between the dominant microstates 2 and 1 that have a high percentage of self-conserved probability (72% for microstate 2 and 85% for microstate 1) reflecting the stability of these macrostates (Figure 8a). Both macrostates featured a stable closed conformation of switch I and moderate variability in the switch II region. The vastly different distribution is obtained for the KRAS-Q61R complex with RAF1, revealing expansion of macrostates and reflecting the increased conformational plasticity of KRAS (Figure 8b). Indeed, we observed that, in addition to the main macrostates 1 and 2, there is a significant population of other macrostates (3, 4, 5, and 6) (Figure 8b). The transition probabilities are especially high between macrostates 1 and "right leg" of the distribution (macrostates 5 and 6). Notably, macrostates 5 and 6 are also found for KRAS-G13D (Figure 8). However, unique to Q61R, the distribution also featured macrostates 3 and 4 with smaller yet appreciable transition probabilities to microstate 2 (Figure 8b). The macrostates 3 and 4 correspond to semi-open intermediate conformations that are not significantly populated in the WT KRAS or other mutant forms of KRAS. Hence, the Q61R mutation partly alters the energy landscape of KRAS, lowering the energy barriers between macrostates and allowing for more frequent transitions between them, which results in a more complex and dynamic conformational landscape (Figure 8b).

The expansion of macrostates induced by the Q61R mutation may have important structural and functional implications for KRAS signaling. The expanded number of macrostates reflects the increased dynamic behavior of KRAS, which may facilitate its interaction with a broader range of effectors. The stabilization of

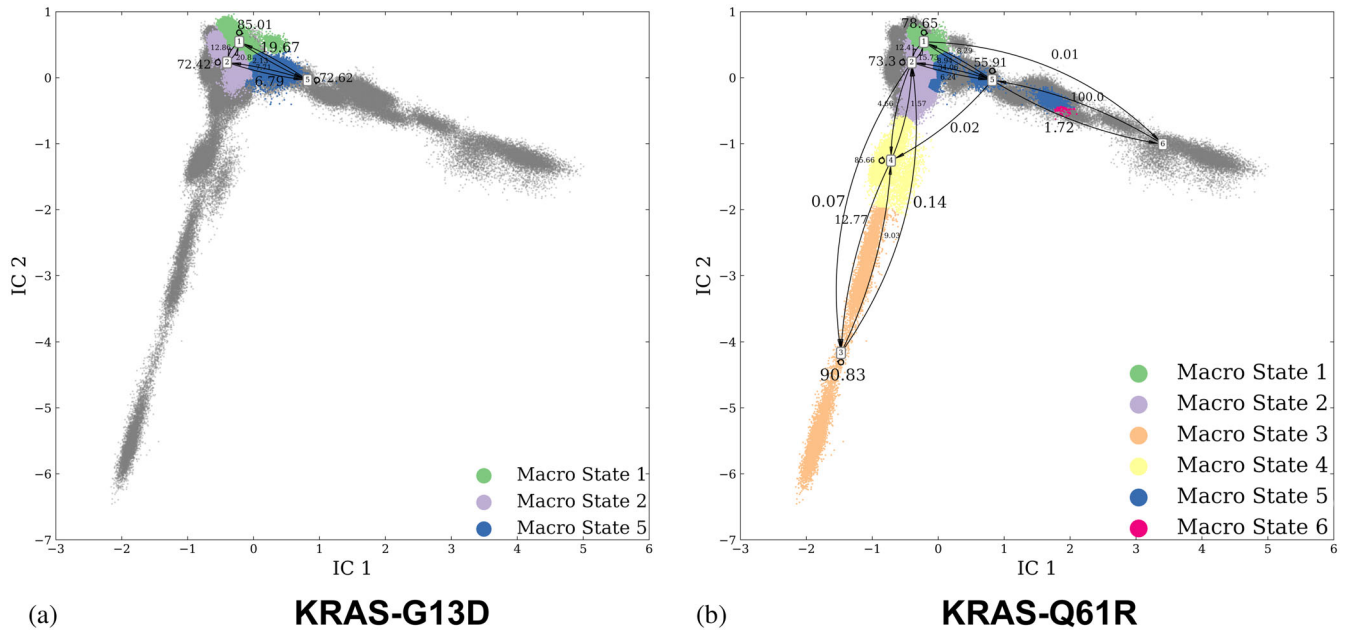

FIGURE 8 Markov state models analysis of the conformational landscape for KRAS-G13D and KRAS-Q61R complexes. The transition probability maps among different macrostates with the 10 ns lag time for KRAS-G13D (a) and KRAS-Q61R complexes (b).

intermediate states and the increased flexibility of switch II may also prolong the interaction between KRAS and RAF1, leading to prolonged signaling and enhancing effector binding. NMR studies of KRAS mutants reveal the dynamic nature of the switch regions and the existence of multiple conformational states (Rennella et al., 2024) consistent with the MSM results.

To conclude, MSM analysis revealed that KRAS mutants may exhibit subtle and yet distinct conformational dynamics signatures compared to KRAS-WT, with stabilization of the active state and altered flexibility of the switch regions.

3.3 | Mutational scanning of KRAS-RAF1 protein binding and stability reveals conserved energy hotspots and effects of oncogenic mutants

Using conformational ensembles obtained from MD simulations, we performed systematic mutational scanning of the KRAS residues in the KRAS-RAF1 complexes (Figure 9). In silico mutational scanning was done by averaging the binding free energy changes over the equilibrium ensembles and allows for predictions of the mutation-induced changes of the binding interactions and the stability of the complex. To provide a systematic comparison, we constructed mutational heatmaps for the KRAS interface residues. We used BeatMusic (Dehouck et al., 2006, 2009, 2013) to identify binding interface residues. Residues are considered part of the interface if they are within a defined cutoff distance (typically 5 Å) from atoms in the binding partner. Our definition of binding interface residues corresponds to the definition of the contact residues in the experimental studies (Weng et al., 2024). The mutational heatmap of the KRAS-RAF1 complex revealed several important binding affinity hotspots that correspond to I36, Y40, R41, and Y64 residues (Figure 9a). The largest destabilization changes are associated with mutations of Y40, including Y40D ($\Delta\Delta G = 2.67$ kcal/mol), Y40S ($\Delta\Delta G = 2.49$ kcal/mol), Y49E ($\Delta\Delta G = 2.45$ kcal/mol) and Y40K ($\Delta\Delta G = 2.3$ kcal/mol) (Figure 9a). Consistent with the free energy experiments (Weng et al., 2024), this simplified model established the importance of the aromatic side chain in the Y40 KRAS position, which makes a cation–π interaction with RAF1 R89 residue. The results of mutational scanning recapitulated subtle experimental data showing that E37D mutation is not tolerated while E37 replacements by Y, F, and H can be tolerated, indicating that the salt bridge to RAF1 R67 can be substituted by interactions involving an aromatic side chain (Figure 9a). Consistent with the functional mutational scanning data (Weng et al., 2024), the mutational heatmap also showed that I21, I36, and S39 are important binding hotspots that make multiple hydrophobic contacts with RAF1 and where polar mutations are highly detrimental (Figure 9a). As was found experimentally, mutations at other interface residues that contact RAF1 are better tolerated, particularly mutations at D33 with only charge-reversing mutations to R and K, and mutation to P mildly inhibiting binding (Figure 9a). Similarly, mutations at the other two charged sites E31 at the edge of the interface have essentially neutral effects on the binding free energy (Figure 9a). The only position

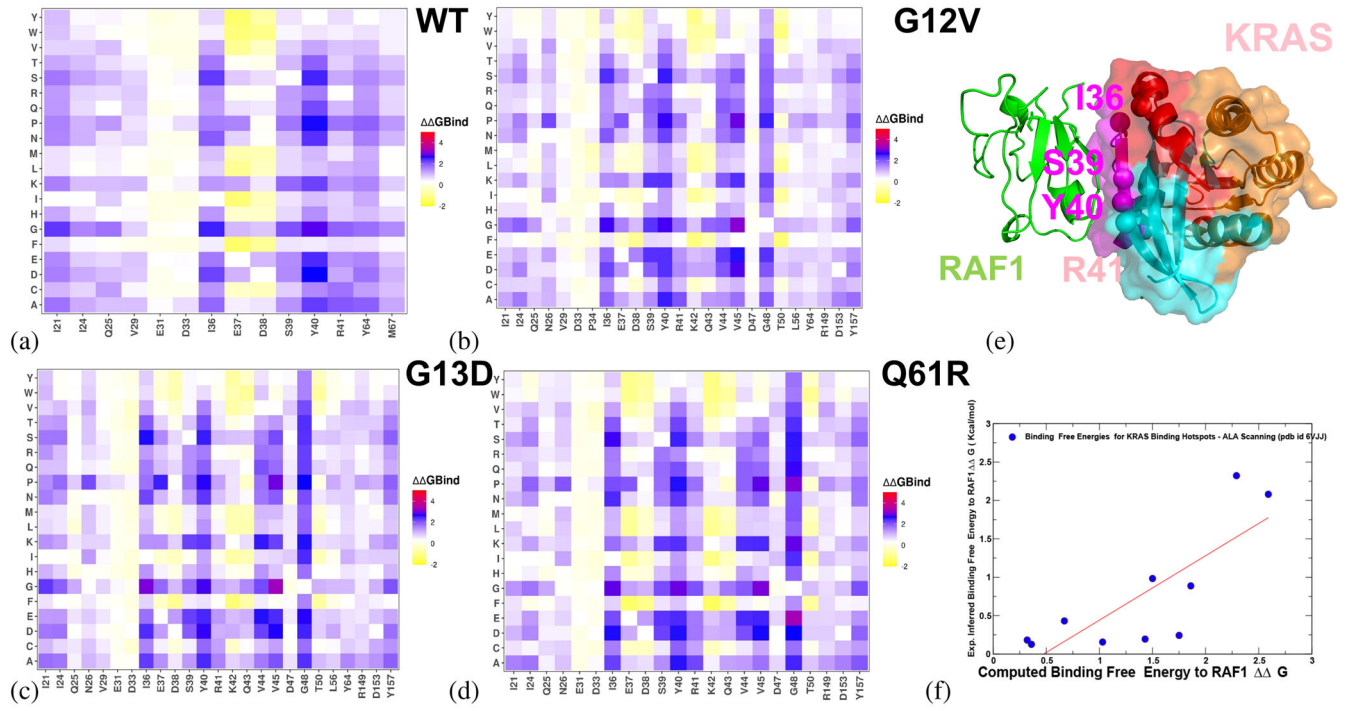

FIGURE 9 Ensemble-based dynamic mutational profiling of the Kirsten rat sarcoma viral oncogene homolog (KRAS) intermolecular interfaces in the KRAS-RAF1 complexes. The mutational scanning heatmaps are shown for the interfacial KRAS residues in the KRAS-wild-type (WT) complex (a), in the KRAS-G12V complex (b), in the KRAS-G13D (c) and KRAS-Q61R complexes (d). The heatmaps show the computed binding free energy changes for 20 single mutations of the interfacial positions. The standard errors of the mean for the binding free energy changes using randomly selected 1000 conformational samples from the molecular dynamics trajectories were 0.11–0.18 kcal/mol. (e) Structural mapping of the binding energy hotspots in the KRAS-WT complex with RAF1. The hotspot positions are shown in red spheres. RBD RAF1 is in green ribbons, SWI is depicted in magenta and SWII region is in red. The allosteric lobe (residues 87–166) is shown in orange. (f) A correlation between experimentally inferred binding energies (Weng et al., 2024) and predicted binding free energy changes for a group of experimentally established KRAS binding hotspots that included residues I21, I24, E31, D33, E37, D38, S39, Y40 and R41.

where mutational scanning disagreed with the experiments is D38, where according to our data, only reversing charge mutations cause detrimental effects while other mutations can be tolerated (Figure 9a). In contrast, the experimental data showed that D38 cannot be changed to any other amino acid without detrimental effects on binding affinity (Weng et al., 2024).

Importantly, we found that the effects of G12V, G13D, and Q61R mutations on the binding affinity and interface residues of RBD RAF1 are relatively moderate. Indeed, the KRAS binding hotspots I36, Y40, and R41 are preserved, but notably, mutations at E37 positions become less tolerant, while modifications at R41 are slightly less detrimental, albeit still unfavorable (Figure 9b–d). While the G13D mutation does not directly alter the E37 and D38 residues in the switch I region, it appeared to enhance their interactions with RAF1 by stabilizing the active conformation of KRAS (Figure 9c). E37 forms a salt bridge with R67 of RAF1 and electrostatic interactions with R59, which is critical for stabilizing the KRAS-RAF1 interaction. Also located in the switch I region, D38 interacts with R67 and R89 of RAF1 through electrostatic interactions. Although the mutational changes in E37 positions of the G13D KRAS complex are not dramatic, they are appreciable and may result from G13D-induced stabilization of the active conformation, which enhances the accessibility of E37 and D38 for interaction with RAF1 (Figure 9c).

Mutational heatmap for the KRAS-Q61R mutant complex displayed generally similar patterns to G13D with some stronger effect on binding of I36 and Y40 and modestly weaker effect on E37 and D38 (Figure 9d). Mutational heatmap for KRAS-Q61R complex showed that key binding hotspots are I36, S39, Y40, and R41 for RBD of RAF1 and additionally V45 and G48 positions that are binding affinity hotspots for interactions with CRD of RAF1 (Figure 9d). In contrast to the KRAS-RBD interface consisting of polar and charged interactions, the KRAS-CRD interface contains no salt bridges and a large hydrophobic interface. KRAS interacts with CRD mainly via its residues present in the inter-switch region (R41, K42, Q43, V44, V45, I46, D47, and G48) and in the C-terminal helix α5 (R149, D153, and Y157). Mutational heatmaps showed that V44, V45, and G48 are critical hotspots of binding with CRD (Figure 9c,d). V44 interacts with hydrophobic residues in the RBD and CRD of RAF1, such as L154 and V155. The mutational heatmaps pointed also to

KRAS residues R149, D153, and Y157 that are interfacing specifically with the CRD of RAF1 (Figure 9c,d). These residues, located on the C-terminal helix of KRAS in the allosteric lobe, are peripherally positioned relative to the core binding interface with RAF1. However, this region contributes to the overall stability of the KRAS-RAF1 interface. R149 is a positively charged residue that can form electrostatic interactions with acidic residues in the CRD, while D153 is engaged in electrostatic interactions with H175 and R179 of the CRD of RAF1. Mutations at this position (D153A or charge reversal D153K, D153R) disrupt these interactions, reducing binding affinity (Figure 9c,d). Finally, Y157 mutations have stronger detrimental effects on binding affinity as this aromatic residue participates in hydrophobic interactions and hydrogen bond interactions with E174 of the CRD of RAF1 (Figure 9c,d). Overall, the interactions formed by these KRAS residues with CRD are weaker and less significant for binding than those provided by V44, V45, and G48 sites. As a result, mutations in R149, D153, and Y157 are more tolerant to mutations as suggested by the computed heatmaps. These results are consistent with the DMS data (Weng et al., 2024) indicating that besides the KRAS residues present in the inter-switch region, especially residues K42 to V45, play an important role in RAF activation, most likely through KRAS-CRD interactions (Figure 9c,d). Structural mapping of the binding energy hotspots highlighted the central role of switch I residues in mediating interactions with RBD RAF1 (Figure 9e).

We also directly compared the experimental and predicted binding free energy changes for a group of experimentally established KRAS binding hotspots that included residues I21, I24, E31, D33, I36, E37, D38, S39, Y40, and R41 (Figure 9f). This analysis revealed a statistically significant correlation between computed and experimental binding free energy changes, supporting the results and interpretations of computational studies performed in this study.

To enhance a comparative analysis and further validate the predictive ability of the computational model, we also performed structure-based mutational scanning of the KRAS binding interface in other complexes with other binding partners, including KPIK3CG (PDB ID 1HE8) (Figure S6A), RALGDS (PDB ID 1LFD) (Figure S6B), SOS1 (PDB ID 1NVW) (Figure S6C), DARPin K27 (PDB ID 5O2S) (Figure S6D), and DARPin K55 (PDB ID 5O2T) (Figure S6E) and compared the results with the experimental data. We first considered how mutations in the binding interfaces alter binding to four additional interaction partners. By comparing mutational effects, we found that some residues, particularly I21, I36, Y40, and Y64, are critically important for binding to all three proteins (Figure S6). For example, many mutations of hydrophobic residues I36 and Y40 strongly inhibit binding to all three effectors. In general, mutational scanning against all partners showed relative tolerance of KRAS residues E31 and D33 and also similar patterns for mutations of more vulnerable positions E37 and D38 (Figure S6). The residues E37 and D38 are shared binding hotspots in KRAS, critical for interactions with RAF1, PIK3CG, and RALGDS. Mutations at these residues (e.g., E37D, E37A, D38A, and D38K) significantly reduce binding affinity, while certain substitutions (e.g., E37Y/F/H and D38E) may be tolerated depending on the binding partner. Mutations of S39 have a stronger effect on binding to PIK3CG and RAF1 but not to RALGDS. Hence, although mutational scanning can accurately and robustly predict major binding affinity hotspots and the effects of most detrimental mutations, the resolution of a simplified knowledge-based energy function may often be insufficient to capture more subtle and sensitive specificity changes, particularly in some polar interface residues.

We additionally examined the free energy changes for KRAS residues that are not involved in the binding interface to identify protein stability hotspots and compare the results with the experiments (Weng et al., 2024). According to the experiments, the major peaks of stability changes in the alanine scanning are associated with KRAS residues K5, L6, V8, G10, G15, K16, S17, F78, L79, V81, I100, M111, V112, D119, T142, T148 (Figure S7A) (Weng et al., 2024). Alanine scanning of all KRAS residues showed that the most detrimental effects on protein stability occur upon mutations of residues F82, K5, L6, V8, G10, F78, L79, V81, V112, L113, V114 (Figure S7). We identified the key stability centers in the P-loop as well as F78, L79, and V81 positions that are part of the hydrophobic core of KRAS, which is essential for maintaining the protein's overall stability and folding. Our results showed that disruption of F78, L79, and V81 residues from this region through mutation to alanine destabilizes the hydrophobic core, leading to reduced stability of KRAS (Weng et al., 2024) (Figure S7). Overall, the results suggested that mutations detrimental to folding are enriched in the hydrophobic core of the protein and successfully reproduced the experimental stability hotspots (Weng et al., 2024).

3.4 | MM-GBSA analysis of the binding energetics provides quantitative characterization of thermodynamic drivers of protein interactions

Using the conformational equilibrium ensembles obtained from MD simulations of the KRAS-RAF1 WT and KRAS mutant complexes, we computed the binding free energies for these complexes using the MM-GBSA method. MM-GBSA is employed to (a) decompose the free energy contributions to the binding free energy on a per-residue basis; (b) evaluate the role of hydrophobic and electrostatic interactions in KRAS-RAF1 binding; (c) identify the binding energy hotspots and compare MM-GBSA

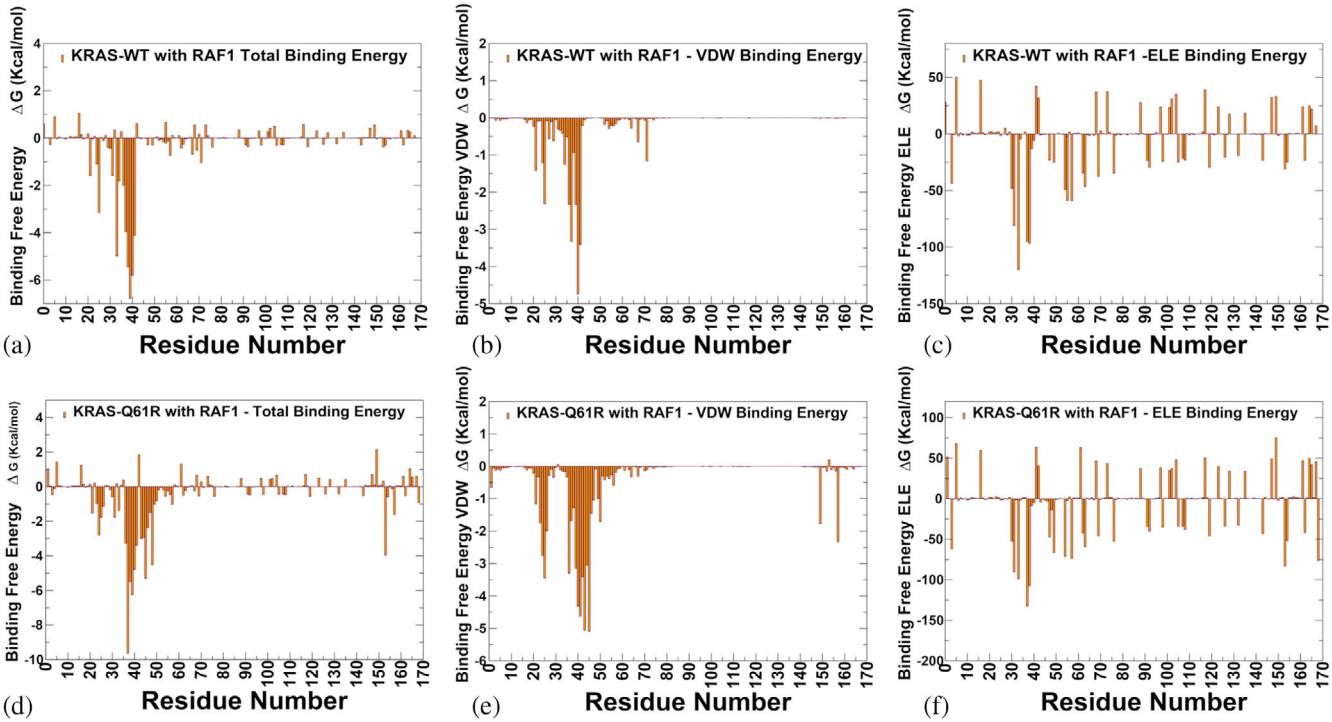

FIGURE 10 The residue-based decomposition of the total binding molecular mechanics generalized Born surface area (MM-GBSA) energies for the Kirsten rat sarcoma viral oncogene homolog (KRAS) residues in the KRAS-wild-type (WT) complex with RAS-binding domain (RBD) RAF1 (a) and KRAS-Q61 mutant (d). The residue-based decomposition of the van der Waals contribution to the total MM-GBSA binding energy for the KRAS residues in the KRAS-WT complex with RBD RAF1 (b) and KRAS-Q61R mutant (e). The residue-based decomposition of the electrostatic contribution to the total MM-GBSA binding energy for the KRAS residues in the KRAS-WT complex with RBD RAF1 (c) and KRAS-Q61R mutant (f). The MM-GBSA contributions are evaluated using 1000 samples from the equilibrium molecular dynamics simulations of the respective KRAS-RAF1 complexes. It is assumed that the entropy contributions for binding are similar and are not considered in the analysis.

predictions with mutational scanning analysis. We started with the MM-GBSA analysis of the KRAS-WT complex (Figure 10a–c). The energy decomposition showed that the binding affinity hotspots correspond to switch I residues S39 ($\Delta G = -6.77$ kcal/mol), Y40 ($\Delta G = -5.8$ kcal/mol), D38 ($\Delta G = -5.45$ kcal/mol), D33 ($\Delta G = -4.98$ kcal/mol), R67 ($\Delta G = -4.77$ kcal/mol) and R41 ($\Delta G = -4.1$ kcal/mol) (Figure 10a). The analysis of the van der Waals contributions pointed to a critical role of this binding energy component for hotspot Y40 ($\Delta G_{VDW} = -4.74$ kcal/mol), R41 ($\Delta G_{VDW} = -3.41$ kcal/mol), and E37 ($\Delta G_{VDW} = -3.33$ kcal/mol) (Figure 10b). Of significance is the contribution of electrostatic interactions, as some major binding hotspots of KRAS correspond to the charged residues E37, D38, D33, E168, and D57 (Figure 10c). MM-GBSA calculations suggested that the van der Waals and electrostatic interactions can be synergistic to yield the most favorable binding energies for Y40, E37, D38, S39, and R41 hotspots (Figure 10a). These results are in agreement with DMS studies (Weng et al., 2024) showing that the critical interface residues include a mixture of charged (E37 and D38) and hydrophobic (I36 and Y40) residues. Y40 forms hydrophobic interactions and a cation–π interaction with R89 of RAF1. E37 forms a salt bridge with R67 of RAF1, and this electrostatic interaction is critical for stabilizing the switch I region and enhancing binding affinity (Figure 10a–c).

For comparison, we also analyzed the energy decomposition for the KRAS-Q61R mutant complex with RB-CRD of RAF1 (Figure 10d–f). The key binding affinity hotspots with RBD of RAF1 in this complex are E37 ($\Delta G = -9.64$ kcal/mol), S39 ($\Delta G = -6.25$ kcal/mol), D38 ($\Delta G = -6.25$ kcal/mol), and Y40 ($\Delta G = -4.78$ kcal/mol) (Figure 10d). In addition, the results revealed top binding hotspots for KRAS binding with CRD of RAF1, which are V45 ($\Delta G = -5.31$ kcal/mol) and G48 ($\Delta G = -4.52$ kcal/mol) (Figure 10d). The most favorable van der Waals interactions are formed by R41, Y40, I36, and S39 with RBD of RAF1, while V45 binding to CRD is driven primarily by the strongest van der Waals contacts (Figure 10e). Similar to KRAS-WT, KRAS-Q61R binding to RBD is driven by strong electrostatic interactions of switch I residues E37, D38, and D33, as well as another strong interacting center D57 from β-strand 3. Hence, consistent with the experiments, our results similarly established that the central β-sheet plays a key role in modulating KRAS activity and particularly mediating allosteric binding with RAF1 (Figure 10f).

Similar energetic patterns and the same binding hotspots emerged from MM-GBSA computations of the

KRAS-G13D complex with RBD-CRD of RAF1 (Figure S8). To sum up, a comparison of MM-GBSA energies for KRAS-WT, KRAS-G13D, and KRAS-Q61R mutant complexes indicated that a conserved pool of major KRAS binding centers from switch I, particularly E37, D38, and Y40, are dominant binding affinity hotspots shared among studied KRAS mutants.

We also performed MM-GBSA mutational scanning of the key interfacial residues E31, D33, E37, D38, S39, Y40, and R41 in the KRAS-WT complex with RAF1 (Figure S9A). The results clearly showed significant destabilizing changes upon all mutations of key binding hotspot residues D33, E37, D38, and Y40. Mutational scanning underscored the role of electrostatic interactions as the dominant contribution of D33 to the KRAS-RAF1 binding interface (Figure S9B). D33 forms a salt bridge with K84 of RAF1, which is a strong electrostatic interaction, and electrostatic contacts with N71. As a result, the electrostatic interactions serve as the primary thermodynamic driver of the D33 binding hotspot, and the disruption of these interactions, particularly by charge reverse mutations D33K and D33R, reduces binding affinity significantly, which is precisely what was found experimentally (Weng et al., 2024). Similarly, MM-GBSA-based mutational scanning of the E37 hotspot reflected the role of strong salt bridges formed by E37 with R59 and R67 residues on RBD RAF1 (Figure S9C). The interactions of E37 with R67 and R59 stabilize switch I region, which is critical for high-affinity binding to RAF1. This stabilization ensures that the switch I region adopts the proper conformation for interaction with RAF1. In addition, the largest destabilizing energy changes upon mutations were observed for two major hotspots, D38 (Figure S9D) and Y40 (Figure S9F). D38 makes strong electrostatic interactions with R67 and R89 and also favorable van der Waals contacts with A85, T68, and V69 of RAF1. As a result, such mutations as D38Q, D38K, and D38V result in large destabilization changes (Figure S9D). This is consistent with experiments showing that D38 cannot be changed to any other amino acid without detrimental effects on binding affinity (Weng et al., 2024). Similarly, Y40 forms highly favorable cation–π interaction with RAF1 R89 residue, as well as favorable contacts with V88 and Q66 of RAF1. For the Y40 hotspot, mutations Y40K and Y40R also produced large destabilizing changes (Figure S9F). MM-GBSA analysis and mutational scanning showed that the hotspots can be grouped in the top tier (E37, D38, and Y40) and secondary tier (E31 and S39).

To summarize, MM-GBSA analysis highlights the synergistic role of electrostatic and hydrophobic interactions in stabilizing the KRAS-RAF1 complex. Residues lY40 and E37 contribute to binding through both types of interactions, underscoring the importance of a balanced interplay between these forces. The results also revealed the critical role of switch I residues D33, E37, D38, and Y40 in binding to RAF1. The MM-GBSA predictions are in excellent agreement with experimental data (Weng et al., 2024) underscoring the reliability of MM-GBSA for identifying binding energy hotspots and thermodynamic drivers of protein–protein interactions. The MM-GBSA-based mutational scanning results provide insights into the effects of specific mutations on KRAS-RAF1 binding, particularly charge-reversal mutations (e.g., D33K, D33R, D38K, and Y40K) that significantly destabilize the complex, highlighting the importance of electrostatic interactions. MM-GBSA results are also consistent with mutational scanning produced by simplified energy models. Both approaches revealed conserved binding hotspots (E37, D38, and Y40) across KRAS-WT, KRAS-Q61R, and KRAS-G13D proteins.

3.5 | Probing allostery in the KRAS-RAF1 complexes using dynamic network analysis: allosteric landscape of KRAS binding and hotspots of allosteric communications

We used the ensemble-based network centrality analysis and the network-based mutational profiling of allosteric residue propensities that are computed using the topological network parameter SPC to characterize the global network of allosteric communications. Through ensemble-based averaging over mutation-induced changes in the SPC metric, we identify KRAS positions in which mutations on average cause network changes. Allosteric hotspots are identified as residues in which mutations incur significant perturbations of the global residue interaction network that disrupt the network connectivity and cause a significant impairment of global network communications and compromise signaling. By performing the in silico version of "deep" mutational scanning to measure the allosteric effects in the KRAS-RAF1, we examine the variant-induced network changes. Using a graph-based network model of residue interactions, we first computed the ensemble-averaged distributions of the residue-based SPC metric (Figure 11a). SPC is a measure of the influence of a node in a network based on the number of shortest paths that pass through it. Nodes with high betweenness centrality function as bridges or bottlenecks in the network, facilitating communication between different parts of the network. The distributions revealed several critical clusters of residues that are important for mediating allosteric communications, particularly concentrated in regions (residues 6–8, 15–25, 35–43, 53–60, 75–80, 95–100, and 115–120) (Figure 11a). These important for allosteric communication sites include residues from P-loop, switch-I, switch-II, β-strand 4: 77–84, α-helix 3: 87–104, and β-strand 5: 109–115. The dominant peaks correspond to residues L6, I55, G15,

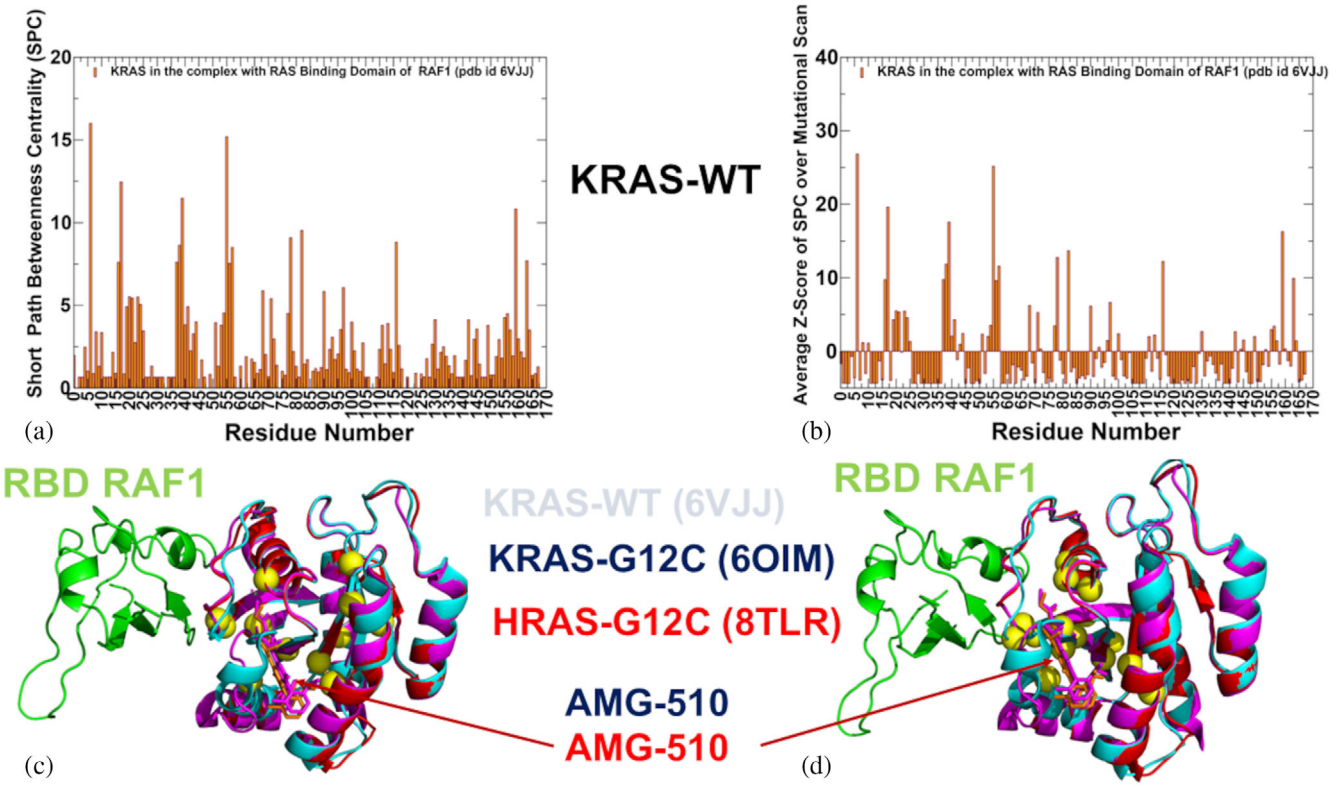

FIGURE 11 (a) The ensemble-averaged short path betweenness (SPC) centrality for the Kirsten rat sarcoma viral oncogene homolog (KRAS) residues in the KRAS-wild-type (WT) complex with RAF1 (in orange filled bars). (b) The SPC peaks (G15, K16, S17, E37, D38, S39, I55, D57, M72, F78, H95, Y96, and R97 residues) defining potential allosteric centers are shown in yellow spheres and mapped onto the crystal structure of the KRAS-RAF1 complex (PDB ID 6VJJ). The KRAS-WT is in cyan ribbons. The KRAS-RAF1 complex is overlayed with the structures of human KRAS-G12C bound with allosteric inhibitor AMG-510 (blue ribbons, AMG50 is in blue sticks) and human HRAS-G12C bound to AMG-510 (red ribbons, AMG-510 is in red sticks). (c) The *Z*-score of SPC centrality for KRAS residues averaged over mutational scan for each residue (in orange filled bars). (d) Structural mapping of the predicted Z-score peaks and assigned allosteric hotspots with KRAS positions S17, S39, L159, F82, F78, N116, D38 D57, R97, and R68 shown in yellow spheres. The structures of KRAS-RAF1 (cyan ribbons), human KRAS-G12C complex (blue ribbons) and HRAS-G12C complex (red ribbons) are shown along with the bound allosteric inhibitor AMG-510. HRAS, human RAS.

K16, S17, E37, D38, S39, D57, M72, F78, H95, Y96, and R97 (Figure 11a).

By mapping these sites onto the crystal structure of the KRAS-RAF1 complex, we found that the predicted allosteric centers are lined up to form major allosteric communication routes connecting the KRAS core with the KRAS-RAF1 binding interface (Figure 11b). One group of residues is located in a small groove that is known to be occupied by allosteric inhibitors, while another cluster consists of key binding interface residues from switch I (E37, D38, S39, and Y40). Strikingly, the predicted allosteric cluster that is distant from the RAF1 binding interface consists of KRAS residues (H95, Y96, and R97) forming a cryptic allosteric pocket that is targeted by the known allosteric inhibitor sotorasib (AMG-510) (Berta et al., 2023).

Indeed, structural studies showed that the isopropyl-methylpyridine substituent of AMG-510 occupied the His95 groove engaged in a network of primarily van der Waals contacts extending from the backbone of helix 2 (H95 and Y96) to the flexible switch II loop (Figure S10). The recent illuminating study from Shokat lab used structural and pharmacological analysis of members of the Ras, Rho, and Rab family of GTPases to demonstrate that this cryptic allosteric pocket in the switch II region of KRAS can be present in other GTPases, indicating that GTPases exhibit targetable allosteric binding pockets (Morstein et al., 2024). We also examined the Z-score of SPC centrality for RBD residues averaged over a mutational scan for the KRAS residues (Figure 11c). In this model, we characterize residues where mutations on average induce a significant increase in the SPC metric and therefore have a dramatic effect on the efficiency of long-range communications in the allosteric interaction network. This analysis enables identification of allosteric control points that could determine the efficient and robust long-range communications in the KRAS-RAF1 complexes. The profile further highlighted the major peaks in which mutational perturbations cause significant changes in allosteric communications. The emerging dominant peaks corresponded to KRAS positions L6, I55, S17,

S39, L159, F82, F78, N116, D38, D57, R97, and R68 (Figure 11c). The structural map of *Z*-score peaks that define in this model potential allosteric centers reveal a dominant allosteric route connecting the central core of KRAS with the switch II region in the binding interface, while several residues, including R68, Y96, and R97, are nestled in a more peripheral cryptic pocket targeted by allosteric drugs (Figure 11d). Notably, the network analysis did not explicitly compute the mutational effects in these allosteric centers on the binding affinity with RAF1 but rather on the efficiency of allosteric communications. Nonetheless, the striking revelation of the network analysis is that the majority of the predicted hotspots were also experimentally determined as allosteric binding hotspots (Weng et al., 2024). More specifically, among 18 experimentally identified allosteric binding centers that are distant from the binding interface with RAF1 and yet significantly affect the binding affinity of KRAS are D57, G15, K16, S17, T35, F28, Y32, and P34 positions (Weng et al., 2024).

Of particular significance are allosteric hotspots D57, G15, and S17 that are away from the binding interface. The network-based allosteric analysis identifies these sites as major hotspots of allosteric communication that affect interaction paths from remote parts of KRAS to the binding interface (Figure 11b,d). These findings suggest that the efficiency of long-range communication between a given remote site and binding interface measured by profiling of the SPC metric is linked with the effect of this site on binding as mutations in the allosteric site can induce perturbations at the binding interface and thus impair binding with RAF1. One of the most striking findings of the experimental studies of KRAS allostery is the efficient propagation of allosteric effects across the central β-sheet of KRAS, which acts as a hub for transmitting conformational changes linking distant functional sites (Weng et al., 2024). Consistent with these experimental findings, structural mapping of the predicted allosteric centers showed a significant population across the central β-sheet of KRAS. Indeed, the predicted hotspots L6 is from β-strand 1 (3–9), E37, D38, S39, Q43 belong to β-strand 2 (38–44), and I55, L56, D57 belong to β-strand 3 (51–57) (Figure 11b,d).

Hence, the network-based modeling of allosteric interactions in KRAS-RAF1 complexes identified critical clusters of residues important for allosteric communication, including residues from the P-loop, switch I, switch II, β-strand 4 (77–84), α-helix 3 (87–104), and β-strand 5 (109–115). In agreement with the experiments, our results similarly established that the central β-sheet plays a key role in modulating KRAS activity and particularly mediating allosteric binding with RAF1. The predicted allosteric centers form major communication routes connecting the KRAS core with the KRAS-RAF1 binding interface (Figure 11d). These routes connect the KRAS core with the switch I regions through a small groove occupied by allosteric inhibitors using the central β-sheet of KRAS for transmitting conformational changes and linking distant functional sites. These visualizations emphasize connectivity between functionally important allosteric residues and regions, highlighting the role of the central β-sheet as a hub for transmitting allosteric signals between distant functional sites. Key residues in these routes include L6 (β-strand 1), E37, D38, S39 (switch I region), Q43 (β-strand 2), and I55, L56, D57 (β-strand 3). The predicted allosteric hotspots align with experimentally identified allosteric binding centers, such as D57, G15, K16, S17, T35, F28, Y32, and P34. These residues, although distant from the binding interface, significantly affect binding affinity with RAF1. The results also highlight the importance of allosteric communication in KRAS that is mediated by a network of residues that function as bridges or bottlenecks in the allosteric network. Mutations in these residues disrupt allosteric communication and impair KRAS-RAF1 binding, highlighting their importance for maintaining KRAS function.

4 | DISCUSSION

MD simulations of KRAS-WT and its oncogenic mutants (G12V, G13D, and Q61R) in complex with RAF1 provided interesting insights into the comparative structural dynamics and binding mechanisms of KRAS. These simulations revealed how oncogenic mutations alter the dynamic behavior of KRAS. The switch I region displays considerable flexibility in KRAS-WT, fluctuating between semi-open and closed conformations, whereas oncogenic mutations tend to generally restrict fluctuations of switch I and favor the stable closed conformation, which is productive for RAF1 binding. Consistent with the NMR experiments (Rennella et al., 2024), we found Q61R leads to a complete shift toward the active state and behaves differently from the other oncogenic mutations at the G12 and G13 positions. MD simulations combined with the MSM analysis detailed how oncogenic mutations (G12V, G13D, and Q61R) stabilize the active conformation of KRAS, enhancing its binding affinity for RAF1. Our results showed that the Q61R mutation induces a more complex conformational landscape, characterized by the reduced flexibility of the active form of switch I, coupled with increased switch II flexibility and expansion of functional macrostates. These changes in allosteric communication highlight the importance of switch II as a mediator of KRAS dynamics and signaling.

The integration of BeAtMuSiC and MM-GBSA provides a hierarchical and quantitative atomistic characterization of KRAS binding determinants. BeAtMuSiC offers a high-level, residue-specific identification of

"binding affinity hotspots" by leveraging statistical potentials derived from large structural databases, enabling the rapid prioritization of critical residues that significantly impact binding stability. This hierarchical approach identifies key regions of interest at the interface. Complementing this, MM-GBSA delivers a detailed, physics-based decomposition of binding free energies into their enthalpic components (van der Waals, electrostatic, and solvation contributions), offering a quantitative atomistic view of the specific interaction types driving binding. Together, these methods create a comprehensive framework: BeAtMuSiC highlights where binding is most sensitive to perturbation, while MM-GBSA explains how these interactions achieve stabilization at the molecular level. This dual approach ensures both a broad understanding of hotspot residues and a precise quantification of the thermodynamic drivers, enabling a robust and nuanced characterization of KRAS binding determinants. Mutational scanning and MM-GBSA analysis identified key binding affinity hotspots at the KRAS-RAF1 interface, including Y40, E37, D38, and D33. The results from BeAtMuSiC and MM-GBSA were integrated to ensure robustness and reliability. For example, residues identified as binding affinity hotspots by BeAtMuSiC (e.g., Y40, E37, D38, and D33) were consistently found to make significant contributions to binding energetics in the MM-GBSA analysis. Furthermore, MM-GBSA revealed that these hotspots often derive their contributions through synergistic electrostatic and hydrophobic interactions, underscoring the importance of a balanced interplay between these forces.

Network-based modeling further identified allosteric hotspots, such as D57, G15, and S17, which influence binding affinity despite being distant from the interface. These findings align with experimental studies and showed that mutations at these sites can significantly affect KRAS-RAF1 binding free energy. The central result of the network analysis is that the central β-sheet region of KRAS acts as a hub for transmitting allosteric signals, facilitating communication between the nucleotide-binding site, effector-binding site, and distant functional regions. The consistency between our computational findings and experimental results underscores the utility of integrating these approaches to study KRAS dynamics and guide therapeutic development. While the computational studies presented in this work provide valuable insights into the allosteric regulatory landscapes of KRAS and its interactions with RAF1, there are several limitations that must be acknowledged. These limitations stem from the inherent challenges of modeling complex biomolecular systems and the approximations used in computational methods. These include timescale limitations of MD simulations, simplifications in MSM and network models, approximate energy functions in free energy calculations. Although the computational predictions align well with available experimental data, there are still gaps in the experimental validation of certain predictions, particularly for allosteric hotspots and long-range communication pathways. For example, the predicted allosteric role of residues like D57 and G15 is supported by indirect evidence, but direct experimental validation (e.g., through mutagenesis or NMR relaxation experiments) is needed to confirm their functional importance. The timescales of MD simulations (nanoseconds to microseconds) are often much shorter than the timescales of experimental techniques (e.g., NMR relaxation and single-molecule fluorescence resonance energy transfer), which can measure dynamics on the millisecond to second timescale. This discrepancy can make it challenging to directly compare computational and experimental results. Despite these limitations, the findings of this study provide a strong foundation for understanding the allosteric regulation of KRAS and its interactions with RAF1.

The detailed understanding of binding and allosteric landscapes for KRAS mutants presented in this study has implications for the design of next-generation inhibitors and therapeutic strategies. One promising avenue is the targeting of cryptic allosteric pockets, such as the switch-II/α3 pocket and the H95/Y96 pocket, which transiently form during conformational fluctuations. Small molecules or biologics designed to stabilize these pockets could lock KRAS in an inactive state, preventing effector interactions and downstream signaling. This approach is particularly relevant for oncogenic mutants like G12V, G13D, and Q61R, which exhibit unique dynamic signatures and altered conformational ensembles. Our findings also highlight the importance of developing mutant-specific inhibition strategies. For instance, G12V stabilizes switch II while subtly reducing flexibility in other regions, whereas Q61R rigidifies switch I and enhances switch II flexibility. These differences suggest that inhibitors tailored to the specific interaction profiles of each mutant may achieve higher selectivity and efficacy. By leveraging the thermodynamic drivers of binding identified through MM-GBSA analysis, researchers can prioritize key residues and interaction types for drug design. Furthermore, the central β-sheet of KRAS acts as a hub for transmitting allosteric signals between distant functional sites, including the nucleotide-binding site, switch regions, and the RAF1 binding interface. Targeting allosteric hotspots, such as D57, G15, and S17, could disrupt KRAS-RAF1 binding and inhibit oncogenic signaling. Combination therapies targeting multiple regions of KRAS, such as the nucleotide-binding site and the allosteric switch-II/α3 pocket, could also mitigate the risk of resistance mutations emerging at single hotspots.

Based on the findings presented in this study, several avenues for future research could be proposed to further advance our understanding of KRAS and inform therapeutic development. Future studies should

incorporate explicit membrane models to investigate how membrane orientation and lipid composition influence KRAS dynamics and allosteric effector binding, providing a more physiologically relevant context for KRAS behavior. The detailed atomistic-level information on the binding affinity hotspots, allosteric centers, and cryptic pockets in KRAS can be leveraged for robust targeted screening of allosteric modulators and mutation-specific inhibitors. In addition, the network-based modeling of allosteric communication pathways revealed key residues that act as bottlenecks or bridges in the network. Experimental validation of these findings, such as through site-directed mutagenesis or NMR studies, would strengthen the mechanistic understanding of KRAS allosteric mechanisms and inform rational drug targeting of KRAS interactions.

5 | CONCLUSIONS

Through an integrative approach combining microsecond MD simulations, MSM analysis, computational mutational scanning, MM-GBSA binding free energy calculations, and network modeling, we have elucidated several key findings. We found that oncogenic mutations differentially modulate this dynamic behavior. G12V rigidifies switch II, while the Q61R mutation uniquely stabilizes the closed conformation of switch I while increasing the flexibility of switch II, enhancing RAF1 binding. These findings provide a mechanistic understanding of how specific mutations contribute to oncogenic outcomes and highlight the importance of targeting mutant-specific conformations for therapeutic development.

Computational mutational scanning and MM-GBSA analysis identified key binding affinity hotspots, including Y40, E37, D38, and D33, which stabilize the KRAS-RAF1 complex through synergistic electrostatic and hydrophobic interactions. These residues may represent potential targets for therapeutic intervention. The analysis of allosteric communication networks revealed that the central β-sheet region of KRAS acts as a hub for transmitting allosteric signals between distant functional sites, facilitating communication between the nucleotide-binding site, effector-binding site, and regulatory regions. Key allosteric hotspots, such as D57, G15, and S17, were identified, where mutations or structural perturbations can dramatically affect KRAS-RAF1 binding affinity. The results of this study provide important quantitative insights into principles of allosteric communication and allosteric binding in KRAS that are consistent with the experimental data, particularly showing that allosteric communication is mediated by conserved positions across the central β-sheet region of KRAS.

AUTHOR CONTRIBUTIONS

Sian Xiao: Methodology; validation; visualization; software; formal analysis; data curation; investigation. **Mohammed Alshahrani:** Investigation; methodology; validation; visualization; software; formal analysis; data curation. **Guang Hu:** Investigation; methodology; validation; visualization; writing – original draft; software; formal analysis; data curation; resources. **Peng Tao:** Investigation; writing – original draft; methodology; validation; visualization; software; formal analysis; data curation; resources. **Gennady Verkhivker:** Conceptualization; investigation; funding acquisition; writing – original draft; methodology; validation; visualization; writing – review and editing; software; formal analysis; project administration; data curation; supervision; resources.

ACKNOWLEDGMENTS

Gennady Verkhivker acknowledges support from Schmid College of Science and Technology at Chapman University for providing computing resources at the Keck Center for Science and Engineering.

FUNDING INFORMATION

This research was supported by the National Institutes of Health under Award 1R01AI181600-01 and Subaward 6069-SC24-11 and the Kay Family Foundation Grant A20-0032 to Gennady Verkhivker and the National Institutes of Health under Award No. R15GM122013 to Peng Tao.

CONFLICT OF INTEREST STATEMENT

The authors declare no conflict of interest. The funders had no role in the design of the study; in the collection, analyses, or interpretation of data; in the writing of the manuscript; or in the decision to publish the results.

DATA AVAILABILITY STATEMENT

Data are fully contained within the article and Supporting Information S1. Crystal structures were obtained and downloaded from the Protein Data Bank (http://www.rcsb.org). The rendering of protein structures was done with the UCSF ChimeraX package (https://www.rbvi.ucsf.edu/chimerax/) and Pymol (https://pymol.org/2/). The software tools used in this study are freely available on GitHub sites https://github.com/smu-tao-group/protein-VAE; https://github.com/smu-tao-group/PASSer2.0. All the data obtained in this work (including simulation trajectories, topology and parameter files, the software tools, and the in-house scripts) are freely available at ZENODO at https://zenodo.org/records/13989093.

ORCID

Peng Tao https://orcid.org/0000-0002-2488-0239
Gennady Verkhivker https://orcid.org/0000-0002-4507-4471

REFERENCES

Alawieh D, Cysique-Foinlan L, Willekens C, Renneville A. RAS mutations in myeloid malignancies: revisiting old questions with novel insights and therapeutic perspectives. Blood Cancer J. 2024;14:72. https://doi.org/10.1038/s41408-024-01054-2

Ancy I, Penislusshiyan S, Ameen F, Chitra L. Microsecond molecular dynamics simulation to gain insight into the binding of MRTX1133 and trametinib with KRASG12D mutant protein for drug repurposing. J Mol Recognit. 2024;37:e3103. https://doi.org/10.1002/jmr.3103

Baussand J, Kleinjung J. Specific conformational states of Ras GTPase upon effector binding. J Chem Theory Comput. 2013;9:738–49. https://doi.org/10.1021/ct3007265

Berta D, Gehrke S, Nyíri K, Vértessy BG, Rosta E. Mechanism-based redesign of GAP to activate oncogenic Ras. J Am Chem Soc. 2023;145(37):20302–10. https://doi.org/10.1021/jacs.3c04330

Bowman GR. A tutorial on building Markov state models with MSMBuilder and coarse-graining them with BACE. Methods Mol Biol. 2014;1084:141–58. https://doi.org/10.1007/978-1-62703-658-0_8

Bowman GR, Bolin ER, Hart KM, Maguire BC, Marqusee S. Discovery of multiple hidden allosteric sites by combining Markov state models and experiments. Proc Natl Acad Sci U S A. 2015;112:2734–9. https://doi.org/10.1073/pnas.1417811112

Bowman GR, Huang X, Pande VS. Using generalized ensemble simulations and Markov state models to identify conformational states. Methods. 2009;49:197–201. https://doi.org/10.1016/j.ymeth.2009.04.013

Bowman GR, Noé F. Software for building Markov state models. Adv Exp Med Biol. 2014;797:139. https://doi.org/10.1007/978-94-007-7606-7_11

Brinda KV, Vishveshwara S. A network representation of protein structures: implications for protein stability. Biophys J. 2005;89:4159–70. https://doi.org/10.1529/biophysj.105.064485

Canon J, Rex K, Saiki AY, Mohr C, Cooke K, Bagal D, et al. The clinical KRAS(G12C) inhibitor AMG-510 drives anti-tumour immunity. Nature. 2019;575:217–23. https://doi.org/10.1038/s41586-019-1694-1

Chao FA, Chan AH, Dharmaiah S, Schwieters CD, Tran TH, Taylor T, et al. Reduced dynamic complexity allows structure elucidation of an excited state of KRASG13D. Commun Biol. 2023;6:594. https://doi.org/10.1038/s42003-023-04960-6

Chao F-A, Dharmaiah S, Taylor T, Messing S, Gillette W, Esposito D, et al. Insights into the cross talk between effector and allosteric lobes of KRAS from methyl conformational dynamics. J Am Chem Soc. 2022;144:4196–205. https://doi.org/10.1021/jacs.2c00007

Chen CC, Er TK, Liu YY, Hwang JK, Barrio MJ, Rodrigo M, et al. Computational analysis of KRAS mutations: implications for different effects on the KRAS p.G12D and p.G13D mutations. PLoS One. 2013;8:e55793. https://doi.org/10.1371/journal.pone.0055793

Chen J, Wang J, Yang W, Zhao L, Hu G. Conformations of KRAS4B affected by its partner binding and G12C mutation: insights from GaMD trajectory-image transformation-based deep learning. J Chem Inf Model. 2024;64:6880–98. https://doi.org/10.1021/acs.jcim.4c01174

Chen J, Wang J, Yang W, Zhao L, Zhao J, Hu G. Molecular mechanism of phosphorylation-mediated impacts on the conformation dynamics of GTP-bound KRAS probed by GaMD trajectory-based deep learning. Molecules. 2024;29:2317. https://doi.org/10.3390/molecules29102317

Chen J, Zeng Q, Wang W, Hu Q, Bao H. Q61 mutant-mediated dynamics changes of the GTP-KRAS complex probed by Gaussian accelerated molecular dynamics and free energy landscapes. RSC Adv. 2022;12:1742–57. https://doi.org/10.1039/d1ra07936k

Clementel D, Del Conte A, Monzon AM, Camagni GF, Minervini G, Piovesan D, et al. RING 3.0: fast generation of probabilistic residue interaction networks from structural ensembles. Nucleic Acids Res. 2022;50:W651–6. https://doi.org/10.1093/nar/gkac365

Dehouck Y, Gilis D, Rooman M. A new generation of statistical potentials for proteins. Biophys J. 2006;90:4010–7. https://doi.org/10.1529/biophysj.105.079434

Dehouck Y, Grosfils A, Folch B, Gilis D, Bogaerts P, Rooman M. Fast and accurate predictions of protein stability changes upon mutations using statistical potentials and neural networks: PoPMuSiC-2.0. Bioinformatics. 2009;25:2537–43. https://doi.org/10.1093/bioinformatics/btp445

Dehouck Y, Kwasigroch JM, Rooman M, Gilis D. BeAtMuSiC: prediction of changes in protein-protein binding affinity on mutations. Nucleic Acids Res. 2013;41:W333–9. https://doi.org/10.1093/nar/gkt450

Del Conte A, Camagni GF, Clementel D, Minervini G, Monzon AM, Ferrari C, et al. RING 4.0: faster residue interaction networks with novel interaction types across over 35,000 different chemical structures. Nucleic Acids Res. 2024;52:W306–12. https://doi.org/10.1093/nar/gkae337

Fernandes HS, Sousa SF, Cerqueira NMFSA. VMD store—a VMD plugin to browse, discover, and install VMD extensions. J Chem Inf Model. 2019;59:4519–23. https://doi.org/10.1021/acs.jcim.9b00739

Fernandez-Fuentes N, Zhai J, Fiser A. ArchPRED: a template based loop structure prediction server. Nucleic Acids Res. 2006;34:W173–6. https://doi.org/10.1093/nar/gkl113

Fetics SK, Guterres H, Kearney BM, Buhrman G, Ma B, Nussinov R, et al. Allosteric effects of the oncogenic RasQ61L mutant on Raf-RBD. Structure. 2015;23:505–16. https://doi.org/10.1016/j.str.2014.12.017

Floyd RW. Algorithm 97: shortest path. Commun ACM. 1962;5:345. https://doi.org/10.1145/367766.368168

Grant BJ, Skjaerven L, Yao XQ. The Bio3D packages for structural bioinformatics. Protein Sci. 2021;30:20–30. https://doi.org/10.1002/pro.3923

Hagberg AA, Schult DA, Swart PJ. Exploring network structure, dynamics, and function using NetworkX. In: Varoquaux G, Vaught T, Millman J, editors. Proceedings of the 7th Python in Science Conference (SciPy2008). SciPy Proceedings; 2008. p. 11–5.

Haliloglu T, Bahar I. Adaptability of protein structures to enable functional interactions and evolutionary implications. Curr Opin Struct Biol. 2015;35:17–23. https://doi.org/10.1016/j.sbi.2015.07.007

Hou T, Wang J, Li Y, Wang W. Assessing the performance of the MM/PBSA and MM/GBSA methods. 1. The accuracy of binding free energy calculations based on molecular dynamics simulations. J Chem Inf Model. 2011;51:69–82. https://doi.org/10.1021/ci100275a

Huang L, Guo Z, Wang F, Fu L. KRAS mutation: from undruggable to druggable in cancer. Signal Transduct Target Ther. 2021;6:386. https://doi.org/10.1038/s41392-021-00780-4

Kolch W, Berta D, Rosta E. Dynamic regulation of RAS and RAS signaling. Biochem J. 2023;480(1):1–23. https://doi.org/10.1042/bcj20220234

Kollman PA, Massova I, Reyes C, Kuhn B, Huo S, Chong L, et al. Calculating structures and free energies of complex molecules: combining molecular mechanics and continuum models. Acc Chem Res. 2000;33:889–97. https://doi.org/10.1021/ar000033j

Koukos PI, Glykos NM. Grcarma: a fully automated task-oriented interface for the analysis of molecular dynamics trajectories. J Comput Chem. 2013;34:2310–2. https://doi.org/10.1002/jcc.23381

Krivov GG, Shapovalov MV, Dunbrack RL Jr. Improved prediction of protein side-chain conformations with SCWRL4. Proteins. 2009;77:778–95. https://doi.org/10.1002/prot.22488

Kwon JJ, Dilly J, Liu S, Kim E, Bian Y, Dharmaiah S, et al. Comprehensive structure-function analysis reveals gain- and loss-of-function mechanisms impacting oncogenic KRAS activity. bioRxiv. 2024 https://doi.org/10.1101/2024.10.22.618529

Lee JK, Sivakumar S, Schrock AB, Madison R, Fabrizio D, Gjoerup O, et al. Comprehensive pan-cancer genomic landscape of KRAS altered cancers and real-world outcomes in solid tumors. NPJ Precis Oncol. 2022;6:91. https://doi.org/10.1038/s41698-022-00334-z

Li ZL, Prakash P, Buck M. A "tug of war" maintains a dynamic protein-membrane complex: molecular dynamics simulations of C-Raf RBD-CRD bound to K-Ras4B at an anionic membrane. ACS Cent Sci. 2018;4:298–305. https://doi.org/10.1021/acscentsci.7b00593

Li Y, Zhang Y, Großerüschkamp F, Stephan S, Cui Q, Kötting C, et al. Specific substates of Ras to interact with GAPs and effectors: revealed by theoretical simulations and FTIR experiments. J Phys Chem Lett. 2018;9:1312–7. https://doi.org/10.1021/acs.jpclett.8b00342

Lu J, Bera AK, Gondi S, Westover KD. KRAS switch mutants D33E and A59G crystallize in the state 1 conformation. Biochemistry. 2018;57:324–33. https://doi.org/10.1021/acs.biochem.7b00974

Lu S, Jang H, Gu S, Zhang J, Nussinov R. Drugging Ras GTPase: a comprehensive mechanistic and signaling structural view. Chem Soc Rev. 2016;45:4929–52. https://doi.org/10.1039/c5cs00911a

Lu S, Jang H, Nussinov R, Zhang J. The structural basis of oncogenic mutations G12, G13 and Q61 in small GTPase K-Ras4B. Sci Rep. 2016;6:21949. https://doi.org/10.1038/srep21949

Ma Q, Zhang W, Wu K, Shi L. The roles of KRAS in cancer metabolism, tumor microenvironment and clinical therapy. Mol Cancer. 2025;24:14. https://doi.org/10.1186/s12943-024-02218-1

Maier JA, Martinez C, Kasavajhala K, Wickstrom L, Hauser KE, Simmerling C. ff14SB: improving the accuracy of protein side chain and backbone parameters from ff99SB. J Chem Theory Comput. 2015;11:3696–713. https://doi.org/10.1021/acs.jctc.5b00255

Martin AJ, Vidotto M, Boscariol F, Di Domenico T, Walsh I, Tosatto SC. RING: networking interacting residues, evolutionary information and energetics in protein structures. Bioinformatics. 2011;27:2003–5. https://doi.org/10.1093/bioinformatics/btr315

Miller BR III, McGee TD Jr, Swails JM, Homeyer N, Gohlke H, Roitberg AE. MMPBSA.Py: an efficient program for end-state free energy calculations. J Chem Theory Comput. 2012;8:3314–21. https://doi.org/10.1021/ct300418h

Mir SA, Nayak B, Aljarba NH, Kumarasamy V, Subramaniyan V, Dhara B. Exploring KRas protein dynamics: an integrated molecular dynamics analysis of KRas wild and mutant variants. ACS Omega. 2024;9:30665–74. https://doi.org/10.1021/acsomega.4c02671

Mongan J, Simmerling C, McCammon JA, Case DA, Onufriev A. Generalized born model with a simple, robust molecular volume correction. J Chem Theory Comput. 2007;3:156–69. https://doi.org/10.1021/ct600085e

Morstein J, Bowcut V, Fernando M, Yang Y, Zhu L, Jenkins ML, et al. Targeting Ras-, Rho-, and Rab-family GTPases via a conserved cryptic pocket. Cell. 2024;187:6379–6392.e17. https://doi.org/10.1016/j.cell.2024.08.017

Naritomi Y, Fuchigami S. Slow dynamics in protein fluctuations revealed by time-structure based independent component analysis: the case of domain motions. J Chem Phys. 2011;134:065101. https://doi.org/10.1063/1.3554380

Nguyen K, López CA, Neale C, Van QN, Carpenter TS, Di Natale F, et al. Exploring CRD mobility during RAS/RAF engagement at the membrane. Biophys J. 2022;121:3630–50. https://doi.org/10.1016/j.bpj.2022.06.035

Olsson MH, Søndergaard CR, Rostkowski M, Jensen JH. PROPKA3: consistent treatment of internal and surface residues in empirical pKa predictions. J Chem Theory Comput. 2011;7:525–37. https://doi.org/10.1021/ct100578z

Ostrem JM, Peters U, Sos ML, Wells JA, Shokat KM. K-Ras(G12C) inhibitors allosterically control GTP affinity and effector interactions. Nature. 2013;503:548–51. https://doi.org/10.1038/nature12796

Pandey D, Roy KK. Decoding KRAS dynamics: exploring the impact of mutations and inhibitor binding. Arch Biochem Biophys. 2025;764:110279. https://doi.org/10.1016/j.abb.2024.110279

Pantsar T, Rissanen S, Dauch D, Laitinen T, Vattulainen I, Poso A. Assessment of mutation probabilities of KRAS G12 missense mutants and their long-timescale dynamics by atomistic molecular simulations and Markov state modeling. PLoS Comput Biol. 2018;14:e1006458. https://doi.org/10.1371/journal.pcbi.1006458

Piovesan D, Minervini G, Tosatto SC. The RING 2.0 web server for high quality residue interaction networks. Nucleic Acids Res. 2016;44:W367–74. https://doi.org/10.1093/nar/gkw315

Prior IA, Hood FE, Hartley JL. The frequency of Ras mutations in cancer. Cancer Res. 2020;80:2969–74. https://doi.org/10.1158/0008-5472.CAN-19-3682

Rennella E, Henry C, Dickson CJ, Georgescauld F, Wales TE, Erdmann D, et al. Dynamic conformational equilibria in the active states of KRAS and NRAS. RSC Chem Biol. 2024;6:106–18. https://doi.org/10.1039/d4cb00233d

Roe DR, Cheatham TE III. PTRAJ and CPPTRAJ: software for processing and analysis of molecular dynamics trajectory data. J Chem Theory Comput. 2013;9:3084–95. https://doi.org/10.1021/ct400341p

Rose PW, Prlic A, Altunkaya A, Bi C, Bradley AR, Christie CH, et al. The RCSB protein data bank: integrative view of protein, gene and 3D structural information. Nucleic Acids Res. 2017;45:D271–81. https://doi.org/10.1093/nar/gkw1000

Salomon-Ferrer R, Case DA, Walker RC. An overview of the Amber biomolecular simulation package. WIREs Comput Mol Sci. 2012;3:198–210. https://doi.org/10.1002/wcms.1121

Scherer MK, Trendelkamp-Schroer B, Paul F, Pérez-Hernández G, Hoffmann M, Plattner N, et al. PyEMMA 2: a software package for estimation, validation, and analysis of Markov models. J Chem Theory Comput. 2015;11:5525–42. https://doi.org/10.1021/acs.jctc.5b00743

Schwantes CR, Pande VS. Improvements in Markov state model construction reveal many non-native interactions in the folding of NTL9. J Chem Theory Comput. 2013;9:2000–9. https://doi.org/10.1021/ct300878a

Sharma AK, Pei J, Yang Y, Dyba M, Smith B, Rabara D, et al. Revealing the mechanism of action of a first-in-class covalent inhibitor of KRASG12C (ON) and other functional properties of oncogenic KRAS by 31P NMR. J Biol Chem. 2024;300:105650. https://doi.org/10.1016/j.jbc.2024.105650

Shima F, Ijiri Y, Muraoka S, Liao J, Ye M, Araki M, et al. Structural basis for conformational dynamics of GTP-bound Ras protein. J Biol Chem. 2010;285:22696–705. https://doi.org/10.1074/jbc.M110.125161

Søndergaard CR, Olsson MH, Rostkowski M, Jensen JH. Improved treatment of ligands and coupling effects in empirical calculation and rationalization of pKa values. J Chem Theory Comput. 2011;7:2284–95. https://doi.org/10.1021/ct200133y

Spoerner M, Herrmann C, Vetter IR, Kalbitzer HR, Wittinghofer A. Dynamic properties of the Ras switch I region and its importance for binding to effectors. Proc Natl Acad Sci U S A. 2001;98:4944–9. https://doi.org/10.1073/pnas.081441398

Spoerner M, Hozsa C, Poetzl JA, Reiss K, Ganser P, Geyer M, et al. Conformational states of human rat sarcoma (Ras) protein complexed with its natural ligand GTP and their role for effector interaction and GTP hydrolysis. J Biol Chem. 2010;285:39768–78. https://doi.org/10.1074/jbc.M110.145235

Spoerner M, Nuehs A, Ganser P, Herrmann C, Wittinghofer A, Kalbitzer HR. Conformational states of Ras complexed with the GTP analogue GppNHp or GppCH2p: implications for the interaction with effector proteins. Biochemistry. 2005;44:2225–36. https://doi.org/10.1021/bi0488000

Srinivasan J, Cheatham TE, Cieplak P, Kollman PA, Case DA. Continuum solvent studies of the stability of DNA, RNA, and phosphoramidate−DNA helices. J Am Chem Soc. 1998;120:9401–9. https://doi.org/10.1021/ja981844

Suárez E, Adelman JL, Zuckerman DM. Accurate estimation of protein folding and unfolding times: beyond Markov state models. J Chem Theory Comput. 2016;12:3473–81. https://doi.org/10.1021/acs.jctc.6b00339

Sultan MM, Pande VS. tICA-Metadynamics: accelerating metadynamics by using kinetically selected collective variables. J Chem Theory Comput. 2017;13:2440–7. https://doi.org/10.1021/acs.jctc.7b00182

Sun H, Duan L, Chen F, Liu H, Wang Z, Pan P, et al. Assessing the performance of MM/PBSA and MM/GBSA methods. 7. Entropy effects on the performance of end-point binding free energy calculation approaches. Phys Chem Chem Phys. 2018;20:14450–60. https://doi.org/10.1039/c7cp07623a

Tian C, Kasavajhala K, Belfon KAA, Raguette L, Huang H, Migues AN, et al. ff19SB: amino-acid-specific protein backbone parameters trained against quantum mechanics energy surfaces in solution. J Chem Theory Comput. 2020;16:528–52. https://doi.org/10.1021/acs.jctc.9b00591

Timar J, Kashofer K. Molecular epidemiology and diagnostics of KRAS mutations in human cancer. Cancer Metastasis Rev. 2020;39:1029–38. https://doi.org/10.1007/s10555-020-09915-5

Tran TH, Chan AH, Young LC, Bindu L, Neale C, Messing S, et al. KRAS interaction with RAF1 RAS-binding domain and cysteine-rich domain provides insights into RAS-mediated RAF activation. Nat Commun. 2021;12:1176. https://doi.org/10.1038/s41467-021-21422-x

Trendelkamp-Schroer B, Wu H, Paul F, Noé F. Estimation and uncertainty of reversible Markov models. J Chem Phys. 2015;143:174101. https://doi.org/10.1063/1.4934536

Trozzi F, Wang X, Tao P. UMAP as a dimensionality reduction tool for molecular dynamics simulations of biomacromolecules: a comparison study. J Phys Chem B. 2021;125:5022–34. https://doi.org/10.1021/acs.jpcb.1c02081

Tu G, Gong Y, Yao X, Liu Q, Xue W, Zhang R. Pathways and mechanism of MRTX1133 binding to KRAS G12D elucidated by molecular dynamics simulations and Markov state models. Int J Biol Macromol. 2024;274:133374. https://doi.org/10.1016/j.ijbiomac.2024.133374

Vatansever S, Erman B, Gümüş ZH. Oncogenic G12D mutation alters local conformations and dynamics of K-Ras. Sci Rep. 2019;9:11730. https://doi.org/10.1038/s41598-019-48029-z

Vatansever S, Erman B, Gümüş ZH. Comparative effects of oncogenic mutations G12C, G12V, G13D, and Q61H on local conformations and dynamics of K-Ras. Comput Struct Biotechnol J. 2020;18:1000–11. https://doi.org/10.1016/j.csbj.2020.04.003

Vijayabaskar MS, Vishveshwara S. Interaction energy based protein structure networks. Biophys J. 2010;99:3704–15. https://doi.org/10.1016/j.bpj.2010.08.079

Webb B, Sali A. Comparative protein structure modeling using MODELLER. Curr Protoc Bioinformatics. 2016;54:5.6.1–5.6.37. https://doi.org/10.1002/cpbi.3

Weng C, Faure AJ, Escobedo A, Lehner B. The energetic and allosteric landscape for KRAS inhibition. Nature. 2024;626:643–52. https://doi.org/10.1038/s41586-023-06954-0

Weng G, Wang E, Chen F, Sun H, Wang Z, Hou T. Assessing the performance of MM/PBSA and MM/GBSA methods. 9. Prediction reliability of binding affinities and binding poses for protein-peptide complexes. Phys Chem Chem Phys. 2019;21:10135–45. https://doi.org/10.1039/c9cp01674k

Weng G, Wang E, Wang Z, Liu H, Zhu F, Li D, et al. HawkDock: a web server to predict and analyze the protein–protein complex based on computational docking and MM/GBSA. Nucleic Acids Res. 2019;47:W322–30. https://doi.org/10.1093/nar/gkz397

Wu H, Paul F, Wehmeyer C, Noé F. Multiensemble Markov models of molecular thermodynamics and kinetics. Proc Natl Acad Sci U S A. 2016;113:E3221–30. https://doi.org/10.1073/pnas.1525092113

Xu S, Long BN, Boris GH, Chen A, Ni S, Kennedy MA. Structural insight into the rearrangement of the switch I region in GTP-bound G12A K-Ras. Acta Crystallogr D Struct Biol. 2017;73:970–84. https://doi.org/10.1107/S2059798317015418

Yang Y, Zhang H, Huang S, Chu Q. KRAS mutations in solid tumors: characteristics, current therapeutic strategy, and potential treatment exploration. J Clin Med. 2023;12:709. https://doi.org/10.3390/jcm12020709

Zhang Y, Doruker P, Kaynak B, Zhang S, Krieger J, Li H, et al. Intrinsic dynamics is evolutionarily optimized to enable allosteric behavior. Curr Opin Struct Biol. 2020;62:14–21. https://doi.org/10.1016/j.sbi.2019.11.002

Zhou ZW, Ambrogio C, Bera AK, Li Q, Li XX, Li L, et al. KRASQ61H preferentially signals through MAPK in a RAF dimer-dependent manner in non-small cell lung cancer. Cancer Res. 2020;80:3719–31. https://doi.org/10.1158/0008-5472.CAN-20-0448

SUPPORTING INFORMATION

Additional supporting information can be found online in the Supporting Information section at the end of this article.

How to cite this article: Xiao S, Alshahrani M, Hu G, Tao P, Verkhivker G. Exploring binding and allosteric energy landscapes for the KRAS interactions with effector proteins using Markov state modeling of conformational ensembles and allosteric network modeling. Protein Science. 2025;34(8):e70228. https://doi.org/10.1002/pro.70228